

Deep ocean long range underwater navigation

Peter N. Mikhalevsky, Brian J. Sperry, Katherine F. Wolfe, Matthew A. Dzieciuch, and Peter F. Worcester

Citation: *The Journal of the Acoustical Society of America* **147**, 2365 (2020); doi: 10.1121/10.0001081

View online: <https://doi.org/10.1121/10.0001081>

View Table of Contents: <https://asa.scitation.org/toc/jas/147/4>

Published by the *Acoustical Society of America*

ARTICLES YOU MAY BE INTERESTED IN

[Source localization in the deep ocean using a convolutional neural network](#)

The Journal of the Acoustical Society of America **147**, EL314 (2020); <https://doi.org/10.1121/10.0001020>

[Estimation of seabed properties and range from vector acoustic observations of underwater ship noise](#)

The Journal of the Acoustical Society of America **147**, EL345 (2020); <https://doi.org/10.1121/10.0001089>

[Nonlinear time-warping made simple: A step-by-step tutorial on underwater acoustic modal separation with a single hydrophone](#)

The Journal of the Acoustical Society of America **147**, 1897 (2020); <https://doi.org/10.1121/10.0000937>

[Machine learning in acoustics: Theory and applications](#)

The Journal of the Acoustical Society of America **146**, 3590 (2019); <https://doi.org/10.1121/1.5133944>

[Ship source level estimation and uncertainty quantification in shallow water via Bayesian marginalization](#)

The Journal of the Acoustical Society of America **147**, EL339 (2020); <https://doi.org/10.1121/10.0001096>

[Seabed and range estimation of impulsive time series using a convolutional neural network](#)

The Journal of the Acoustical Society of America **147**, EL403 (2020); <https://doi.org/10.1121/10.0001216>



**Advance your science and career
as a member of the
ACOUSTICAL SOCIETY OF AMERICA**

[LEARN MORE](#)



Deep ocean long range underwater navigation

Peter N. Mikhalevsky,^{1,a)} Brian J. Sperry,¹ Katherine F. Wolfe,¹ Matthew A. Dzieciuch,² and Peter F. Worcester²

¹Leidos, Inc., 4001 North Fairfax Drive, Suite 700 Arlington, Virginia 22203, USA

²Scripps Institution of Oceanography, University of California, San Diego, La Jolla, California 92093-0225, USA

ABSTRACT:

A long range Underwater Navigation Algorithm (UNA) is described that provides a geolocation underwater while submerged without having to surface for a Global Navigation Satellite System (GNSS) position. The UNA only uses measured acoustic travel times from a constellation of underwater acoustic sources analogous to the constellation of satellites in GNSS. The UNA positions are calculated without any *a priori* track, position or sound speed information, and thus provide a “Cold Start” capability. The algorithm was tested using data from the 2010–2011 Philippine Sea Experiment in which six sources were deployed in a pentagon \sim 400 km on a side. 502 positions of hydrophones in a bottom-moored vertical line array at depths of 485–3037 m drifting in a tidal watch circle up to 600 m in diameter were computed. The sources were 129–450 km from the hydrophone receivers. The mean UNA position error from ground truth was 58 m with a standard deviation of 32 m. The UNA Cold Start Algorithm position can be used as the point in the ocean for calculating acoustic model runs from the source positions with a four-dimensional sound speed field from a general circulation model to improve the accuracy.

© 2020 Acoustical Society of America. <https://doi.org/10.1121/10.0001081>

(Received 22 January 2020; revised 23 March 2020; accepted 25 March 2020; published online 20 April 2020)

[Editor: James F. Lynch]

Pages: 2365–2382

I. INTRODUCTION

Navigation underwater has been a problem of great interest going back to World War II with the discovery of the deep sound channel and using Sound Fixing and Ranging (SOFAR) to locate downed aircraft and sinking ships using the acoustic receptions of small explosive charges detonated at the sites to fixed moored undersea hydrophones. In the 1970s, this evolved into the use of subsurface floats with acoustic sources, called SOFAR floats, for measuring subsurface currents, and in the 1980s reversing the acoustic transmissions and having the floats receive acoustic signals from fixed moored acoustic sources. These floats were appropriately called RAFOS floats (SOFAR spelled backwards).¹ “Deep ocean” in the title of this paper refers to the deep sound channel propagation regime.

Improving underwater navigation has become more important with the expanding use of Autonomous Underwater Vehicles (AUVs), buoyancy gliders, and subsurface scientific floats. Undersea navigation today is principally accomplished by requiring subsea vehicles to surface to obtain a Global Navigation Satellite System (GNSS) position. On vehicles equipped with inertial navigation systems (INS), the GNSS position is used to initialize the INS, which provides underwater navigation until the accumulation of inertial error requires surfacing for re-initialization to maintain the desired position accuracy. The best INS systems of the Marine and Navigation grade categories are expensive (from \$100 K to \$1 M+), require more space and power than is available in all but the

very largest AUVs, and are therefore not feasible for use in gliders and floats. Unaided (without GNSS) Tactical and Industrial grade INS systems with size, weight, and power (SWAP) suitable for an AUV have horizontal position errors that are 5 and 53 m after 1 min submerged and 19 and 190 km, after 1 h, respectively.² Surfacing can take time, especially for deep water work, and exposes vehicles/floats to possible adverse weather conditions and compromises stealth. Continuous and accurate (m’s error) underwater navigation is possible with (i) Long Baseline (LBL) systems over ranges of approximately 10 km at specific ocean areas of interest with bottom mounted, surveyed transponders at tens of kHz and (ii) with ship mounted Ultra Short Baseline (USBL) systems over \sim km ranges employing high frequency sources of hundreds of kHz. A review of these and newer technologies for AUV navigation exploiting acoustic ranging (e.g., USBL and LBL) and active imaging and non-acoustic methods with simultaneous localization and mapping (SLAM) technology applied to underwater navigation can be found in Paull *et al.*³ This paper focuses on the long ranges, 100–1000s km applications. RAFOS is currently the state-of-the-art in long range continuous underwater navigation using fixed undersea sources transmitting to subsurface receivers with location uncertainties of 1.5–4.5 km at ranges up to 2000 km, as described by Duda *et al.*⁴

The need for long range underwater navigation in the oceans to basin scales (100–1000s km) was identified by the National Research Council’s (NRC) Committee on an Ocean Infrastructure Strategy for U.S. Ocean Research in 2030, in a report published in 2011. Specifically, the NRC identified the critical infrastructure need for “advancements in underwater navigation for more precise and geodetic

^{a)}Electronic mail: mikhalevskyp@leidos.com

referenced vehicle locations,” and for “permanent, large-scale subsurface acoustic positional networks (analogous to GPS) for improved undersea navigation.”⁵

Previous underwater navigation work exploiting underwater acoustic sources for long-range navigation included tracking buoyancy-driven gliders by Van Uffelen *et al.*⁶ using the 2010–2011 Philippine Sea Experiment source transmissions. This work relied on GNSS at the beginning of the dive and upon resurfacing of the gliders, along with a dynamic model of the glider trajectory while underwater, to provide the position in the ocean with sufficient accuracy to run an acoustic propagation code with an average ocean sound speed calculated from the glider measurements. Time offsets, or the bulk shift between the received source signals on the gliders and the modeled results, were used to generate distance offsets from the estimated glider position, which were used to determine the final geographic position estimate.

Similar work in the Arctic by Webster *et al.*⁷ tracking buoyancy-driven gliders also relied on GNSS, as well as a hydrodynamic model and on board measurements, to estimate the vehicle position and velocity. Acoustic range estimates were based on a high-resolution measured travel time, but there is no discussion of which ray/mode is used in the arrival pattern. The sound speed used to convert the measured travel time to range is the local measured sound speed at the vehicle at the time of reception.

In contrast to these efforts, the Cold Start Algorithm (CSA) (the Underwater Navigation Algorithm Cold Start Algorithm, referred to as UNA CSA or just CSA in this paper) requires no GNSS and no *a priori* sound speed information or any acoustic propagation modeling to obtain the initial geographic position. Furthermore, it is not subject to errors associated with unknown currents that can cause position estimation errors from dynamic vehicle modeling. As such, it would complement the above efforts as another input in a Kalman filter incorporating vehicle dynamics.

An analysis using a simulation of RAFOS tracking by Skarsoulis and Piperakis⁸ included making the soundspeed “*c*” an unknown to be solved for along with the position. However, the travel times used in the simulations had the lower time accuracy (0.2 s) of the RAFOS signals, which cannot resolve the distinct arrival ray/mode peaks. The position errors were always greater and sometimes much greater than 300 m as result of the 0.2-s time resolution. Duda *et al.*⁴ proposed a “RAFOS-2” system for dual usage of navigation of RAFOS floats and acoustic thermometry. They recognized the need for precise travel time measurements of the arrival structure to use for navigation of the floats and for tomographic inversion to improve the accuracy of the sound-speed field. They postulated a RAFOS-2 system with several millisecond travel time resolutions that would be able to locate float positions with a precision of 50 m. Using the more accurate sound speed-fields from the tomographic inversions, they state “there is a potential to locate the drifting floats to an accuracy of 50 m or less...” While Duda *et al.*⁴ was not proposing an underwater navigation system

per se, or providing any navigation algorithms, their speculation of float position errors utilizing tomography is consistent with the performance of the CSA although the latter requires *no a priori* information or tomography.

The next section of the paper, Sec. II, describes the CSA. Section III discusses the testing of the CSA with the data from the 2010–2011 North Pacific Acoustic Laboratory (NPAL) Philippine Sea Experiment,⁹ which will be referred to as “PhilSea10” throughout the paper. Six sources arranged in a pentagon configuration, with one source in the middle, transmitted linear frequency modulation (LFM) waveforms to hydrophones in a bottom-moored, distributed vertical line array (DVLA) receiver (Fig. 1). The sources and the DVLA hydrophones were tracked with bottom deployed transponders to an accuracy of ~1 m. The true position and range error statistics using the ground truth available in PhilSea10 are analyzed and compared to position and range error measures commonly used in GNSS. There were 502 positions computed from 2888 ranges using the DVLA PhilSea10 data. Performance of the CSA throughout the year of the PhilSea10 experiment is discussed. An upper bound on the position error is calculated based on the standard deviation of the group speeds from the PhilSea10 sources. It is the variation of group speed from source to source in underwater navigation that is the fundamental challenge to implement a “GNSS-like” navigation system in the ocean with acoustics.

II. THE CSA

The CSA is a simple robust algorithm that uses travel time measurements from acoustic sources in the ocean that

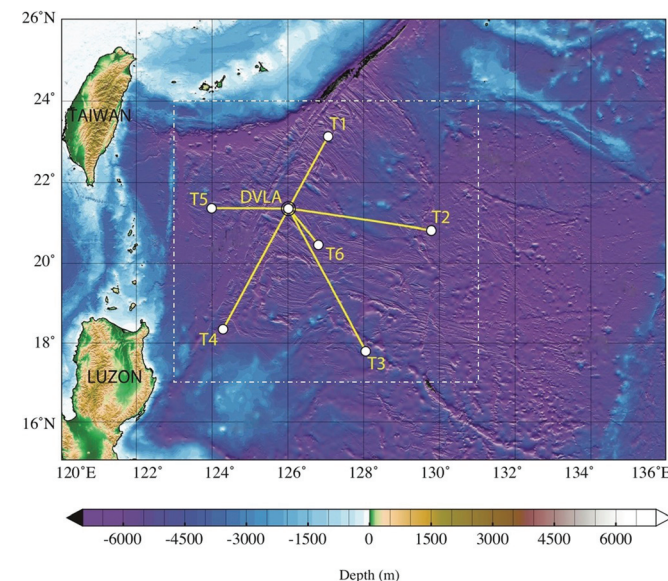


FIG. 1. Geometry of the PhilSea10 experiment. The paths from each of the six broadband sources (T1–T6) to the DVLA are shown. Selected hydrophones on the DVLA at depths from 485 to 3037 m depth were tracked using the received acoustic signals from the sources. The white dashed box is the area for which the 4-D ocean GCM tomographically-constrained model was provided.

are either fixed at known positions or moored and tracked with bottom mounted transponders to compute a geometric position underwater (patent pending¹⁰). The depth of the vehicle being navigated is assumed known with a pressure sensor, so the positioning problem is two-dimensional, requiring the solution of the x , y (Latitude and Longitude) position. The CSA can be implemented with a single hydrophone or vector sensor and an on-board processor with a small SWAP footprint. This makes the CSA suitable for small unmanned underwater vehicles (UUVs), buoys, and floats as well as larger vehicles. The CSA assumes that the source positions are known to ~ 1 m root-mean-square (rms) error in (x , y , and z) and are arranged in a constellation that provides good navigation geometry, namely, source pairs with crossing angles near 90° that result in low Horizontal Dilution of Precision (HDOP)¹¹ approximately equal to or less than 1. HDOP is an uncertainty area calculated for unit standard deviation of the observation range errors and is smallest when source fronts cross at 90° , and grows larger as the crossing angle increases or decreases as the fronts coincide. HDOP is computed exclusively from the source geometry matrix that is the same as the model resolution matrix in other applications. The horizontal position error is the product of HDOP and the standard deviation of the observation range errors from ground truth.¹¹ The CSA requires high bandwidth signals (~ 50 – 100 Hz depending on center frequency) transmitted from the sources with post-pulse compression accuracy of several milliseconds in measuring the multipath/mode arrival times. The PhilSea10 experiment satisfied all these requirements. The HDOP for the PhilSea10 geometry is shown in Fig. 2. The HDOP at the DVLA position is 0.87. In Fig. 2, the latitude and longitude have been converted to an x , y (east and north,

respectively) grid in km with the origin at the DVLA. The hydrophones on the DVLA were used to test the performance of the CSA as the DVLA moved in a diurnal tidal watch circle as much as 600 m in diameter. The CSA position based on the analysis done to date is tolerant (within the current mean position error of ~ 58 m) to absolute timing errors of the vehicle clock of ~ 0.1 – 0.2 s. This makes the CSA feasible for vehicles without very accurate clocks. However, absolute timing accuracy of several ms for the sources and the vehicle is required in order to use high fidelity propagation modeling for improving the CSA position, as discussed in Secs. III C and III E. The development of Chip Scale Atomic Clocks (CSAC) is advancing to the point that millisecond accuracy over a year will be available for AUVs. At this point, the underwater endurance of AUVs is the limit for undersea operations, rather than the accuracy of on-board clocks, for exploiting the CSA capability to remain submerged with navigation. While the UNA CSA was developed for long-range, deep-ocean navigation, the algorithm can be used for any source array topology that provides good HDOP and can bridge the gap between LBL and longer range requirements.

A. CSA detailed description

There are three key components of the CSA that enable the performance achieved to date. The first key component is that the measurement of the “travel time” is the high resolution time measurement (precision of a few milliseconds) of the last path/mode energy detected in the full multipath/multimode arrival pattern or the End of Coda/finale (EOC). A typical multipath/multimode arrival pattern for deep sound channel propagation in the Philippine Sea is shown in Fig. 3 for Julian day 197, 16 July 2010, of the PhilSea10 experiment. The upper panel, Fig. 3(a), shows the amplitude of the pulse-compressed arrival pattern (relative units) and the lower panel, Fig. 3(c), shows the eigenrays between source 6 and a hydrophone in the DVLA at 806 m depth. The eigenrays are computed using the range-dependent Bowlin RAY code¹² with sound speed computed from the four-dimensional (4-D) ocean model for the PhilSea10 experiment constrained by the tomography data.¹³ Figure 3(b) is the range-averaged sound speed between source 6 and the DVLA. The EOC arrival time is not always the last highest peak as shown, for example, in Fig. 3(a). It is the travel-time of the last energy detected that exceeds a pre-selected threshold based on the mean and variance of the noise in the post-pulse compressed time series. Section II B describes the automated EOC travel-time measurement code developed for processing the PhilSea10 data. The second key component of the CSA is a linearized, uniformly weighted least square position estimate (LSE) that solves for the (x , y) position and simultaneously a single sound speed c . The third key component is the combination of the first two, using (i) the measured high temporal resolution EOC travel times from each source and (ii) the inclusion of c as an unknown to be solved for in the least squares solution.

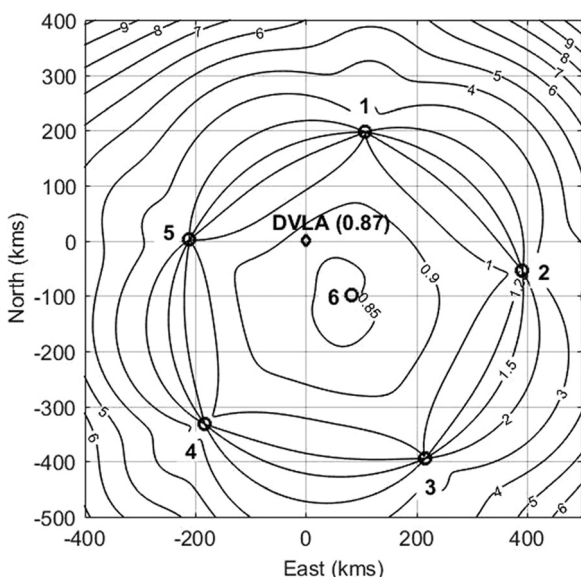


FIG. 2. The HDOP for the geometry of the PhilSea10 sources (numbered 1–6) and DVLA. This is a 2-D line-of-sight calculation without considering actual acoustic propagation effects. HDOP is computed from the geometry matrix in GNSS terminology, also known as the model resolution matrix in other applications.

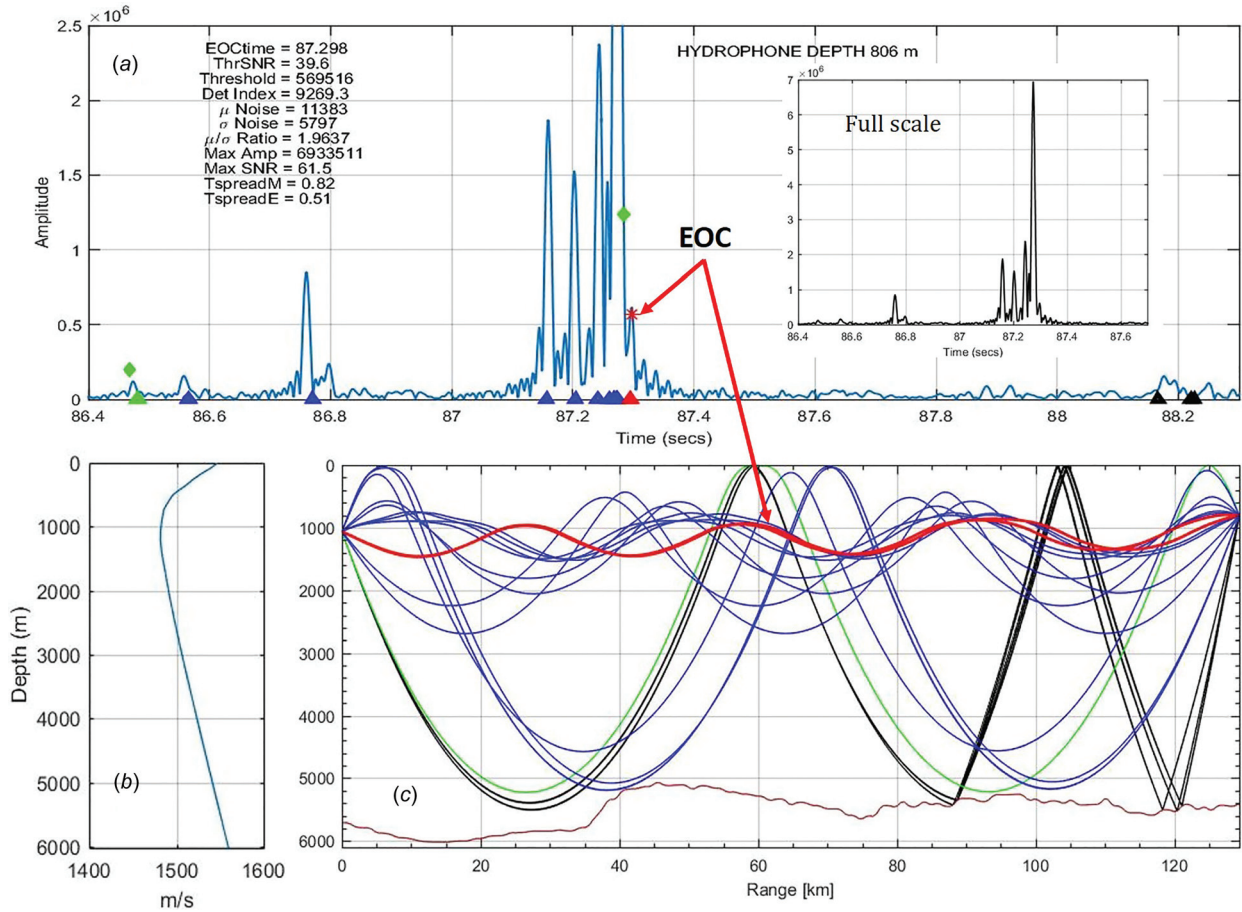


FIG. 3. The upper panel, (a), shows the amplitude of the pulse compressed arrival pattern time series for the transmission from source 6 to the hydrophone in the DVLA at a depth of 806 m on day 197, 16 July 2010. The inset is the full vertical scale showing the maximum peak. Source 6 is 129 km from the DVLA. An automated detection code (Sec. II B) detects the EOC travel-time (red asterisk) of 87.3 s, as shown in the legend. (b) (Left) is the average sound speed from the source to the receiver, and (c) (right) is the Bowlin RAY code ray trace from the actual source position to the actual hydrophone position using the range-dependent sound speed from the PhilSea10 tomographically-constrained ocean model. The triangles on the x axis of the upper panel mark the travel times for the rays shown in the lower panel and are color coded: Green, for the first arrival, a refracted, surface-reflected (RSR) path, blue, the refracted-refracted (RR) paths, black, bottom bounce paths, and red, the last RR near-axial paths (their arrival time is the measured EOC indicated by the red arrows). The launch angles from the source of the near-axial paths are -2.7° and -2.6° , and their arrival angles at the DVLA are 1.1° and -1.0° , respectively. They are the closest to the sound channel axis with a turning depth at the depth of the hydrophone. Slower rays nearer the axis are not detected as they turn below the depth of the hydrophone.

The observation equation is

$$\rho^k \equiv t^k c = \rho^k + e^k, \quad (1)$$

where P^k is the computed range from the k^{th} source, which will be referred to as the observation range, t^k is the measured EOC travel time, c is the sound speed, ρ^k is the geometric range from the source, e^k is the range error, and

$$\rho^k = \sqrt{(x^k - x)^2 + (y^k - y)^2}, \quad (2)$$

where (x, y) are the true position coordinates, and (x^k, y^k) is the known k^{th} source position.

Following Borre and Strang¹⁴ and Misra and Enge,¹¹ ρ^k is linearized around an initial approximate position (x_0, y_0) and $x_1 = x_0 + \Delta x_1$, $y_1 = y_0 + \Delta y_1$, $c_1 = c_0 + \Delta c_1$, and ρ_0^k is defined as Eq. (2) evaluated at the approximate receiver position, (x_0, y_0) . The numerical subscripts refer to an iteration number. Taking the linear terms of the Taylor expansion of

$\rho^k(x_1, y_1) - t^k c_1$, the K first order linear observation equations are obtained, where K is the total number of sources used to determine the position,

$$\rho_0^k - t^k c_0 - \frac{x^k - x_0}{\rho_0^k} \Delta x_1 - \frac{y^k - y_0}{\rho_0^k} \Delta y_1 - t^k \Delta c_1 + e^k = 0. \quad (3)$$

Rearranging the terms in Eq. (3) and using vector notation gives the standard least squares problem, $\mathbf{Ax} = \mathbf{b} - \mathbf{e}$, where \mathbf{A} is the $K \times 3$ matrix of partial derivatives, $\mathbf{b} = t^k c_0 - \rho_0^k$ and $\mathbf{x}^T = [\Delta x_1 \quad \Delta y_1 \quad \Delta c_1]$. The solution for \mathbf{x} in Eq. (3) is found by using the standard normal equations to minimize the sum of the squared errors to obtain x_1 , y_1 , and c_1 . x_1 , y_1 , and c_1 are then used in Eq. (3) (the subscripts are increased by 1) to obtain x_2 , y_2 , and c_2 . The solution minimizes the error until the n^{th} iteration when Δx_n , Δy_n , and Δc_n result in less than a meter change in the least squares position solution, i.e., $x_n = x_0 + \Delta x_1 + \Delta x_2 + \dots + \Delta x_n$,

and the same expressions for y_n and c_n . Effectively, $\mathbf{x} = 0$ in Eq. (3), and the best least squares fit gives $\mathbf{b} = \mathbf{e} - t^k c_g^{CSA} - \rho_{CSA}^k$, where the first term is P^k , the observation range (or user range, somewhat analogous to a “pseudorange” used in GNSS terminology) that is the product of the measured EOC travel time, t^k , and the best fit “ c ” (c_n), denoted c_g^{CSA} . The subscript “ g ” denotes group velocity as discussed below. The second term is the range from the k th source to the CSA position that is referred to as the “CSA” range. The error, e^k , in Eq. (3) is not the true range error, but represents the error as result of the difference between the single c_g^{CSA} and the actual group speed, c_g^k , of the k th source, due to the spatial and temporal variation of group speed in the ocean. P^k is analogous to a GNSS pseudorange since it has a known error due to the single c_g^{CSA} approximation. In GNSS, the pseudorange is so called, as it has a known error because it does not include the correction for receiver clock error. As discussed above, the CSA is robust to receiver clock error as that error is compensated to some extent by the best fit “ c .” The c_g^k variation from source to source in the constellation is the fundamental difference between underwater navigation and GNSS in the atmosphere and will be examined with the analysis of the true range errors using the ground truth available in the PhilSea10 experiment.

For the PhilSea10 data using the anchor position of the DVLA (<600 m from the true position) as the initial approximate position and $c_0 = 1485$ m/s to start, the algorithm converged in two iterations. When the initial position selected was (1000, 1000) in kilometers and $c_0 = 0$, the algorithm required seven iterations and converged to the same solution. There are three unknowns, so a minimum of three sources is required. In practice, more than three sources are required due to errors in EOC travel times and those associated with using a single “ c ” for all the sources, to provide robustness to source drop out, and to give low HDOP. The five to six sources (source 6 ceased transmissions on Julian day 305, 1 November 2010) available in the PhilSea10 tomography experiment were satisfactory and would likely be necessary for an operational system. The HDOP for the PhilSea10, six-source geometry shown in Fig. 2 is 0.87 at the DVLA array location. The HDOP increased only slightly to 0.93 at the DVLA after source 6 failed leaving the five source geometry, because source 3 was almost on the same azimuth from the DVLA as source 6.

The uniformly weighted least squares is used following GNSS practice for positioning with pseudoranges^{11,14} and for similar reasons. The assumption is that there is no *a priori* information that any one source is providing more accurate or higher quality information than any other source. For the CSA, the received signals must have high enough post-pulse compression signal-to-noise ratio (SNR) to provide a travel time precision of 1–3 ms, and the geometry must provide low HDOP. In a few cases (18 out of 502) with marginal SNR, the EOC detection was captured by a noise peak or obvious outlier, and the source was dropped from the position calculation. There is also the assumption that the errors in the measurements from the different sources are

zero mean, uncorrelated, and identically distributed. These assumptions are not exactly true (just as the assumption of a single “ c ” is not true). The more important questions are how close to being true are they and can the biases and correlations be estimated accurately enough to improve performance. Since ground truth is available, actual error statistics can be computed, and as is shown below, the assumptions work well. The same is true in GNSS, and there is a good discussion of the trade-offs in Misra and Enge.¹¹ All the standard positioning performance estimates of GNSS computed as user range error observation variances times dilution of precision (DOP) values are based on the above assumptions. That said, the application of error estimates in the CSA and travel-time measurement process using EOC (or some other travel time measure) in a weighted least squares or Kalman filter smoother/tracker should improve the performance of the CSA reported herein. No smoothing or tracking has been applied as yet, and each position determined by the CSA is independent from any knowledge of previous positions.

An accurate acoustic model or measurement of “ c ” between each source and the receiver requires knowledge of where the receiver is and an accurate ocean sound-speed model sufficiently sampled in space and time. While an ocean sound speed field might be available *a priori*, the position is not. This is the Cold Start problem that the UNA CSA solves. In contrast to GNSS, where the speed of light is a constant with known corrections for propagation in the ionosphere and troposphere, using a single ocean sound speed as an unknown in the term $t^k c$ in Eq. (1) clearly introduces errors proportional to the differences between the actual group speeds from the sources to the receiver, c_g^k , and the single group speed, c_g^{CSA} . As will be shown below, the position error is a function of the standard deviation of the actual group speeds from source to source. This, of course, is the major difference between underwater navigation using the CSA and GNSS, where the deviation of the speed of light in GNSS from satellite to satellite is accounted for explicitly in the observation equations for the position calculations. Because c is a known constant in GNSS, there are four unknowns that are solved for, the three spatial coordinates and receiver clock error (which adds only a single unknown since this error is the same for all satellites). There is a similar term in the GNSS observation equations to “ $t^k c$,” but with the major difference that c is the constant and the receiver time is the unknown (the vehicle clock error). The pseudorange in GNSS is the range from each satellite using the uncorrected receiver clock prior to the least squares solution. The robustness of the CSA to vehicle clock error noted above is due to the CSA “adjusting” c to partially account for any common receiver clock timing offset; however, this gives a c_g^{CSA} that is physically incorrect. In PhilSea10, all clock drifts in the sources and receivers were measured and accounted for in the data. In Sec. III D, there is a discussion of the c_g^{CSA} and a comparison with modelled and estimated group speeds for PhilSea10. With the ground truth, an estimate of the actual group speed, c_g^k , can be made

by dividing the ground truth range by the measured EOC travel-time, t^k , that is denoted, \hat{c}_g^k . For each of the 2888 range estimates \hat{c}_g^k is computed.

B. Automated detection of the EOC travel time, t^k

Any underwater navigation system must have automated onboard processing for receiving the source transmissions and computing their position and track. An automated EOC detection algorithm was developed for the PhilSea10 data to process the pulse compressed time series of the transmissions from the sources to the hydrophones on the DVLA. The noise amplitude in the pulse compressed time series is Rayleigh distributed since the quadrature components were Gaussian for the most part (>90% of the time). The Rayleigh noise mean, μ_ρ , and standard deviation, σ_ρ , are estimated from ~ 3.5 s of data prior to the earliest arrival. A threshold based on μ_ρ is computed for the detection of the earliest arrival in the arrival pattern [green diamond at beginning of the arrival pattern in Fig. 3(a)]. Two additional thresholds are set for (i) an initial estimate of the nominal end of the arrival pattern [green diamond near the end of the arrival pattern in Fig. 3(a)], and (ii) the final auto-detect EOC travel time [red asterisk in Fig. 3(a)] that is after the final green diamond. These thresholds are based on the noise and the SNR of the maximum peak in the arrival pattern. The EOC thresholds are increased for higher SNR cases to prevent capture of matched filter ringing as the EOC. The inset in Fig. 3(a) shows the full scale of the arrival pattern with the maximum SNR arrival peak of 62 dB (in the legend). The EOC threshold was raised. The measured time spread (time between the green diamonds) was used to limit the search to one-half of the measured time spread after the last green diamond for the EOC. This was effective in eliminating capture of spurious noise peaks and bottom bounce paths. The latter were prevalent for source 6, the closest source at 129 km, as shown in Fig. 3. The threshold formulas were empirically based on measurements from about 10% of the data. The earliest arrival pattern threshold was set at $5\mu_\rho$, or equivalently $\sim 9.6\sigma_\rho$ (for the Rayleigh probability density function (pdf) $\mu_\rho = \sigma_\rho \sqrt{4/\pi - 1} \sim 1.913\sigma_\rho$), which gives a probability of false alarm of $\sim 10^{-8}$ for cases in which the noise quadrature components are Gaussian. At the same time, this threshold is high enough to handle the cases that were not, as indicated by the ratio of μ_ρ/σ_ρ deviating significantly from 1.9. This ratio was computed for all 2888 cases. An example is shown in the legend in Fig. 3(a).

The automated algorithm worked quite well. If noise levels were too high or no signal was apparent, e.g., the maximum peak SNR was less than $5\mu_\rho$ for a particular source transmission, it would be zeroed out, and the position would be computed from the other sources (this occurred 20 times and affected 18 positions). There were cases when manual intervention was used to pick the EOC time, e.g., when the EOC peak arrival was present but below the calculated threshold or it had faded out altogether. This typically resulted in multiple tens of meters of position error without

the manual correction. Out of the 2888 ranges processed, 57 manual corrections that affected 35 of the 502 positions were made. The algorithm could have been improved, reducing manual corrections; however, handling special cases or tuning thresholds for this particular data set did not seem warranted given some of the experiment limitations from the standpoint of optimal navigation, which of course was not the objective of PhilSea10. For example, of the 57 manual corrections, 31 were from the two shallowest hydrophone depths, 11 at 537 m, and 20 at 574 m, and 18 were at the deepest depth of 3037 m (reciprocal depth ~ 400 m). No corrections were required at 735 and 1035 m, and only 8 at 1335 m depth. Inconsistent source illumination at these shallow and deep depths led to low SNRs and increased EOC fading. At the very shallow depths (the shallowest DVLA hydrophone was 180 m), there was loss of all sources in many cases. Modeling confirmed that this was due to convergence zone shadow zones at the DVLA from the axial sources. Modeling using an axial source at 1100 m and a deep source at 4000 m filled in these convergence zone gaps. It is necessary for any useful navigation system to determine source positions in depth and range, as well as required source levels to ensure adequate illumination/SNR and HDOP throughout the desired navigation volume at the receiver. The expected received levels and noise interferers such as passing ships, storms, etc., would affect the details of any automated processing algorithms.

III. PHILIPPINE SEA DATA ANALYSIS

PhilSea10⁹ was used to test the CSA position performance against ground truth and compile error statistics of the position and range errors. Hydrophones in the DVLA at depths from 485 to 3037 m were tracked through the diurnal watch circle using the CSA and the transmissions from the six sources from 25 April 2010 to 25 March 2011. Transmissions occurred every other day starting at 0000Z at three hour intervals, giving eight transmission cycles per day. Each transmission cycle started with source 1 followed by each source in sequence at 9 min intervals, so a complete transmission cycle for all six sources took 45 mins. Therefore, eight positions (one for each of the eight transmission cycles) were calculated per day for at least one hydrophone. On some days, up to six hydrophones were tracked. Figure 4 is an example of the eight positions calculated on Julian day 197, 16 July 2010, for a hydrophone at 565 m depth. The asterisks in the figure are the CSA positions, and the small filled circles are the ground truth location of the hydrophone at the time of transmission of each source, hence the six filled circles. The position of the hydrophone at the time of the transmission of the third source was chosen as the ground truth position, noted by the larger unfilled black circle. The position error, P_e , is defined as the distance from the ground truth (larger circle) to the CSA position (asterisk). In this particular case, the mean of the eight P_e 's of the eight positions was 41 m, and the standard deviation was 22 m. Positions were calculated for 21 days of the PhilSea10 experiment with at least one day

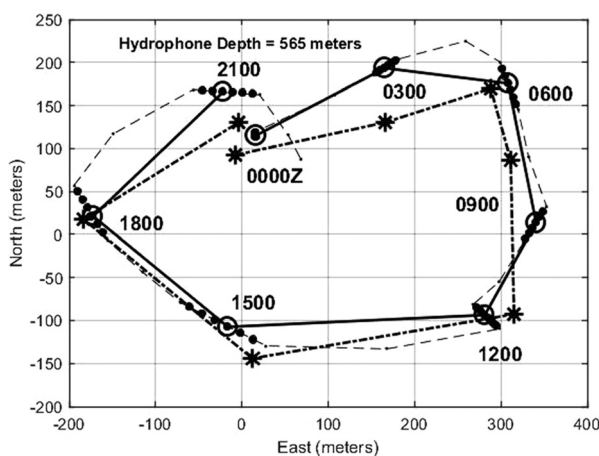


FIG. 4. CSA positions are the asterisks connected by the dotted-dashed line and ground truth are the “O’s” connected by the solid line. The eight transmission sequences start at 0000Z and then every three hours thereafter. The smaller filled circles indicate the transmission time of each of the six sources, with source 1 starting on the hour and subsequent sources at 9 min intervals thereafter. The open circle “O” at the start time of source 3 was defined as the ground truth. The dashed line shows the watch circle of the hydrophone with localization from four bottom transponders every hour. A total of 63 such tracks were computed from the data.

each month. A total of 63 hydrophone plot-tracks like Fig. 4 were generated giving 502 geographic positions (in one of the 63 plot-tracks, two transmission sequences were corrupted and not used), with 2888 source-to-receiver ranges.

The mean of P_e for all the 502 positions was 58 m, with a maximum error of 156 m, a minimum of 1 m, and a standard deviation of 32 m. Figure 5(a) shows a scatter plot of the (x, y) position errors color-coded according to depth. No significant depth dependence of the position errors is evident. The largest deviation from the mean of 58 m for the five depths was 9 m, and the standard deviation for the five depths is 7.5 m. The loss of source 6 did not impact the CSA

performance. 104 positions were calculated after source 6 became inoperative. The mean P_e was 54 m, and the standard deviation was 27 m. As stated earlier, HDOP increased only slightly. For all 502 positions, Fig. 5(b) shows a histogram of P_e that is well modeled by the Rayleigh pdf, passing both the χ^2 and Kolmogorov-Smirnov test at a 0.05 level of significance. This would be expected if the x and y position errors are Gaussian and uncorrelated. They were in fact approximately Gaussian and uncorrelated (with correlation coefficient of 0.1), but did not pass the χ^2 test at a 0.05 confidence level with a mean and standard deviation of (-3 m, 51 m) and (-9 m, 42 m), respectively. In this paper, the mean of P_e has been chosen as the measure of the horizontal or two-dimensional (2-D) position error. In GNSS, the rms horizontal position error, referred to as the 2-D rms error,^{11,15} is defined as the expected value of the sum of the squares of the x and y coordinate errors ($\Delta x, \Delta y$),

$$\text{2-D rms error} = \sqrt{\frac{1}{n} \sum_{i=1}^n (\Delta x_i^2 + \Delta y_i^2)}. \quad (4)$$

For $n = 502$ positions in this dataset, Eq. (4) gives 66 meters. Other measures of horizontal position error have also been widely used in GNSS, including circular error probable (CEP) and horizontal 95% accuracy. The latter two are calculated from the scatter plot [e.g., Fig. 5(a)] and are 65 and 72 m, respectively, for this data set. The 2-D rms error is sometimes represented as synonymous with the standard deviation of the horizontal position error, but this is only true if the x and y coordinate errors are zero mean.¹⁵ Consistent with the facts that the Rayleigh distribution is representative of this data set and the x and y coordinate errors are marginally unbiased, the rms horizontal error can be calculated as the square root of the sum of the x and y error variances,¹¹ and this yields 66 m, in agreement with

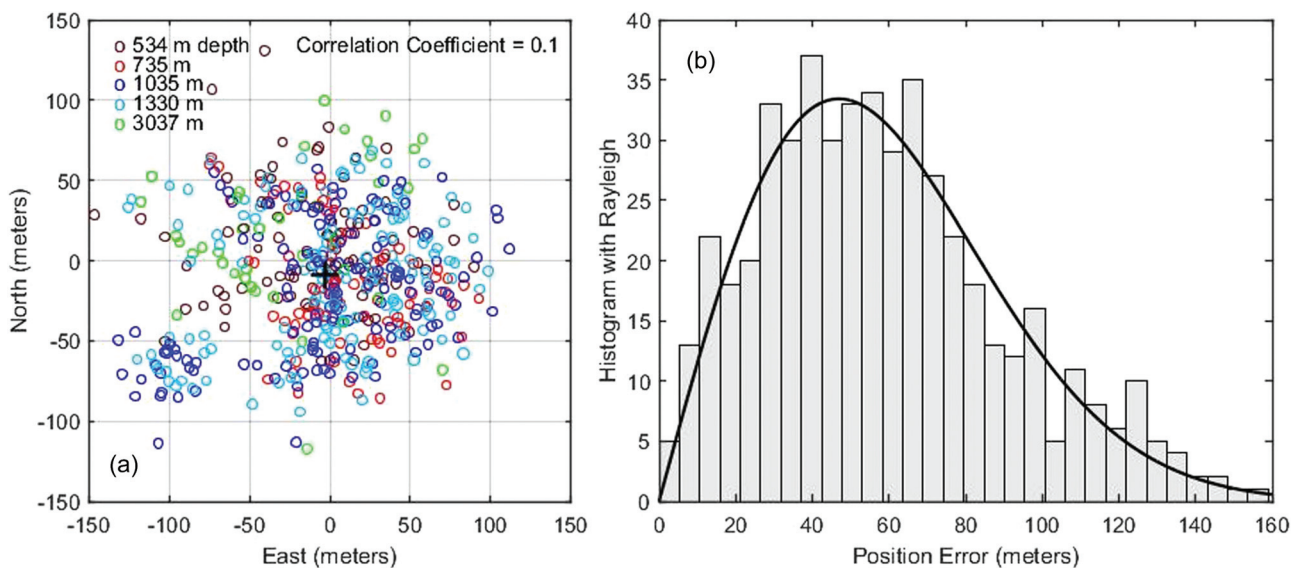


FIG. 5. (a) is a scatter plot of the (x, y) position errors color coded as a function of depth. They are approximately Gaussian and uncorrelated with a mean and standard deviation of (-3 m, 51 m) and (-9 m, 42 m), respectively. Figure 5(b) shows the histogram of the magnitude of the position errors, P_e , (the length of the vector from the origin in (a) to each of the (x, y) coordinate positions in 5(a)] with Rayleigh pdf, using the measured standard deviation of 32 m.

Eq. (4). The GNSS community has not used the Rayleigh mean position error in general, even though the Rayleigh pdf has been shown to model the position errors very well in many, but not all, cases.¹⁶ For our relatively large data set, despite the biased and somewhat marginal fit of the x , y , coordinate errors with the Gaussian, the Rayleigh fit is quite good. If the x and y coordinate errors are normal with zero mean and the same variance, it can be shown that the 2-D rms error is equal to $2/\sqrt{\pi}$ times the mean of the position errors. For this data set with the measured mean of 58 m, this factor gives 65 m for 2-D rms error in agreement with Eq. (4). Thus, Rayleigh mean, 2-D rms, CEP, and horizontal 95% error are equally valid descriptions of “position” error as long as one identifies what they are using.

In Sec. III A, the observation range errors, the CSA range errors, and the least square fit range errors, also known as the residuals, are analyzed to determine their statistics and relationship to the position accuracy using the ground truth. In order to clarify the above range error definitions and geometry, Fig. 6 shows a blow up of the 0600Z transmission on day 197 for the DVLA hydrophone at 726 m depth. The filled circle is ground truth with the known DVLA hydrophone position subtracted and plotted at (0,0), and the “X” is the CSA position. The position error, P_e , is the distance between the ground truth and the CSA position and is 84 m in this case. The angle α is the direction azimuth of the error, 207° in this case. For this data set, α is \sim uniformly distributed between 0° and 360° [Fig. 5(a)]. The range arcs (numbered) from each of the six sources (see Fig. 1) are the product of the measured (observed) EOC

travel time for each source and the CSA group speed, $t^k c_{CSA}^{CSA}$, and are the observation ranges. For this case, the c_g^{CSA} is 1482.13 m/s. The length of the arrow designated “b” in Fig. 6, is the observation range error equal to the observation range for source 3 minus the ground truth range for source 3 (-72.2 m in this case). The observation ranges minus the ground truth ranges will be referred to as the *observation range errors*.

The *CSA range errors* are equal to the CSA ranges minus the ground truth ranges as shown in Fig. 6 for source 3 as the length of the arrow designated “a,” and is equal to -46.9 m in this case.

The least square fit errors or *residuals* are equal to the observation ranges minus the CSA ranges [e , from the solution of Eq. (3)] as illustrated in Fig. 6 for source 3 as “c,” which is -25.3 m in this case. The standard deviation of the residuals is referred to as Least Squares (LS) Sigma in Fig. 6, denoted σ_o , and is 35 m for this CSA position. $\sigma_o = \sqrt{e^T e / (K - 3)}$, namely, the square root of the sum of the squares of the perpendicular offset errors (residuals) for each of the K sources, divided by the degrees of freedom, that is $K - 3$ (K equations / sources and three unknowns). The error ellipse calculated with σ_o at a confidence level of 90% is shown in Fig. 6.

A. Range error statistics and analysis

The histogram of the 2888 observation range errors from ground truth is shown in Fig. 7(a), plotted with a Gaussian pdf using the measured mean of 3.8 m and the measured standard deviation of 77 m. The skewness is -0.33 , and the kurtosis is 4.1, as compared to a skewness of 0 and a kurtosis of 3 for a Gaussian pdf. The standard deviation of the horizontal position error is given by HDOP times the standard deviation of the observed range errors.¹¹ From Fig. 2, HDOP at the DVLA = 0.87 and multiplied by 77 m gives 67 m, which is in agreement with Eq. (4). Thus, HDOP multiplied by the variance of the observation range errors is equal to the 2-D rms position error that equals P_e times $2/\sqrt{\pi}$ as described above.

The CSA ranges from the sources (to the CSA position) are important, as they will be used as the ranges for the acoustic modeling of the arrival pattern. This, in turn, will be compared to the data to determine correction offsets for position accuracy improvement, as discussed in more detail below. With the ground truth, the statistics of the CSA range errors and position errors can be computed. These are important for implementing a weighted least squares estimate, Kalman filter smoothing/tracking, and developing robust correction algorithms for operational positioning and navigation when ground truth is not available. The histogram of the CSA range errors from ground truth is shown in Fig. 7(b) together with a Gaussian pdf using the measured mean of -2.4 m and the standard deviation of 47 m. The skewness is 0.09, and the kurtosis is 3, in good agreement with the Gaussian pdf. For the large number of bins in Fig. 7(b), the χ^2 test failed. However, with six bins, it passed at the 0.05 level of significance. The CSA ranges benefit from

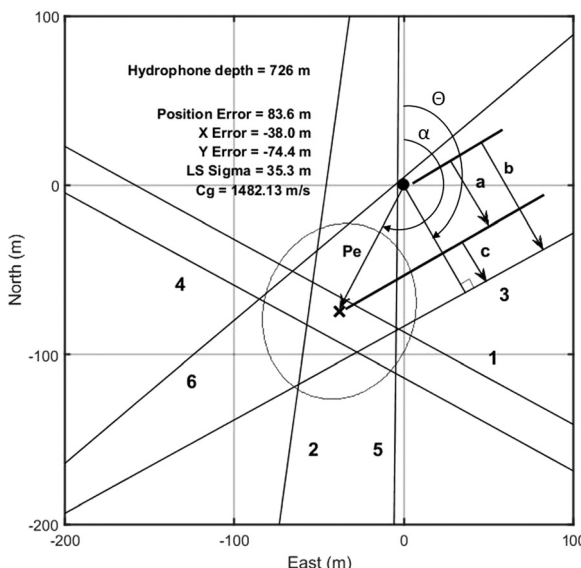


FIG. 6. Blow up of the 0600Z transmission on day 197 with the black filled circle the true position with the ground truth subtracted plotted at (0,0). The “X” is the CSA position. The source range arcs are numbered by source. The three range errors noted by the arrows “a,” “b,” and “c” are the CSA, observation, and least squares fit range errors (residuals), respectively, for source 3. The definitions of these three range errors are described in the text. α is the azimuth angle of the position error. θ is the source azimuth shown for source 3.

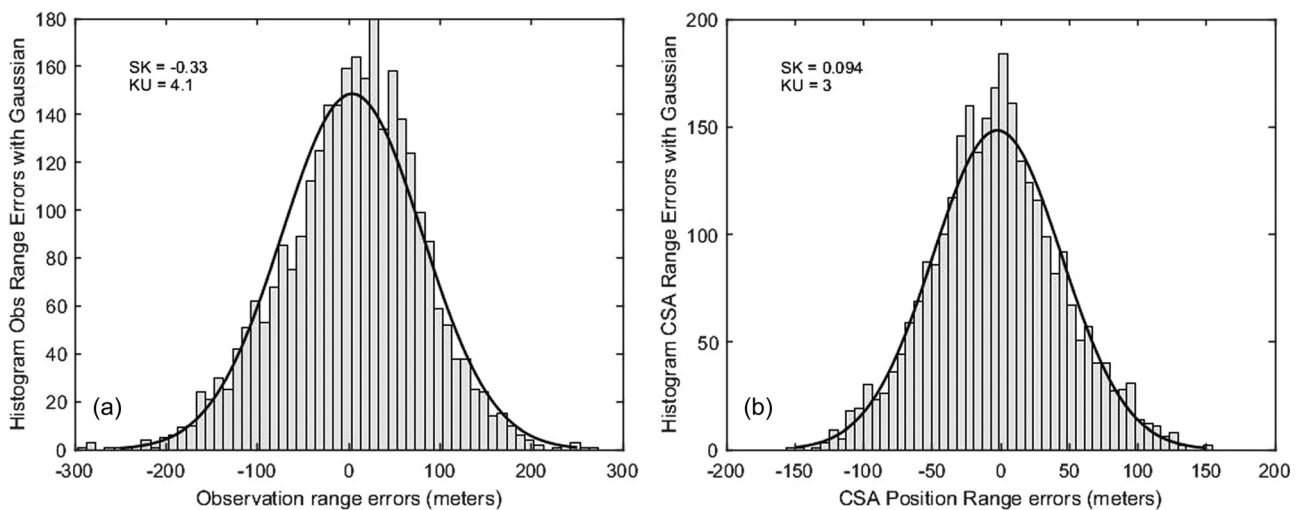


FIG. 7. (a) Shows the histogram of the observation range errors. The Gaussian density is plotted with the measured mean of 3.8 m and measured standard deviation of 77 m. (b) shows the histogram of the CSA range errors. The CSA range errors are Gaussian distributed with the measured mean of -2.4 m and measured standard deviation of 47 m.

the “averaging” of the K source observation ranges used for each of the least squares positions, effectively increasing the number of samples and hence normality by the central limit theorem. Dividing the observation range error standard deviation of 77 m by the square root of the degrees of freedom ($K - 3$), i.e., 2 for the positions after source 6 failed and 3 otherwise, gives 46 m in agreement with measured standard deviation.

The variances of the CSA range errors are independent of range in this data set as shown in Fig. 8, where the range error is plotted as a function of range from the DVLA to each source denoted by the black numbers. In PhilSea10, the sources were from 129 to 450 km from the DVLA. (The position performance as a function of range cannot be computed directly without increasing the range of all sources while maintaining the same HDOP.) Figure 8 shows the means (lower three lines on plot) and standard deviations (upper three lines) of the range errors to each of the sources for the observation range errors (dotted dash) and the CSA range errors (solid line). The mean observation errors are

highly biased exhibiting an erratic trend from longer ranges than actual to shorter ranges as range increases. The standard deviation exhibits an increase with increasing range by a rough factor of the square root of range, but not a strong dependence, and with the variability (20 m rms) it is not certain. The CSA range errors, in contrast, have a much smaller bias with no range trend, and the standard deviation is also independent of range. The means and standard deviations of the residuals, the least squares fit range errors, are also shown in Fig. 8 (the dotted lines), and like the CSA show no range trend in the standard deviation. If this holds up at longer ranges, then one could expect the position performance of the CSA to remain the same as range is increased. Another interpretation is that with 58 m mean position error, any range-dependent factors might not be large enough at 450 km range to exceed this error. Testing the CSA at longer ranges is certainly needed. The fact that the standard deviation of the source range errors is the same for all the sources supports the uniform weighting in the least squares calculation.

The standard deviation of the observation range errors multiplied by HDOP is in good agreement with the 2-D position errors discussed earlier. HDOP multiplied by the standard deviation of the CSA range errors, however, does not give the 2-D position errors. Furthermore, the data analysis has shown that the CSA position error P_e is a function of the standard deviation of the K range errors (and K group speeds) of the K sources used to compute that CSA position. A geometric source constellation position factor related but not the same as HDOP is introduced below to explain this relationship. This analysis will permit estimation of the CSA position performance in the ocean using knowledge of ocean group speed variability (possibly from ocean general circulation models (GCMs) or at-sea experiments) and a source constellation location and geometry.

The standard deviation of the K CSA range errors from the sources used for each of the 502 positions plotted versus the corresponding position error, P_e , is shown in Fig. 9(a).

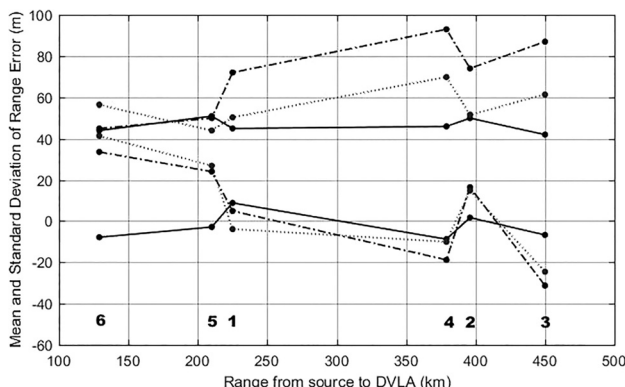


FIG. 8. Means (bottom) and standard deviations (top) of the observation (dotted-dashed), CSA (solid), and residual (dotted) range errors are plotted versus range from the six sources. Black source numbers are plotted at their respective ranges from the DVLA.

There is a linear correlation with the best fit line with a slope of 0.76. By definition, the CSA position range error of each source is the projection of P_e at the error azimuth, α , on the source direction/azimuth, θ (see Fig. 6). The equations for the mean and standard deviation of the CSA position range error, denoted CSAre, of the K sources for each position are

$$\mu_{CSAre} = P_e \frac{1}{K} \sum_{k=1}^K [-\cos(\alpha - \theta(k))], \quad (5)$$

$$\sigma_{CSAre} = P_e \left\{ \frac{1}{K-1} \sum_{k=1}^K \left[-\cos(\alpha - \theta(k)) - \frac{1}{P_e} \mu_{CSAre} \right]^2 \right\}^{1/2}. \quad (6)$$

The sums can be done analytically, and μ_{CSAre} is a one cycle sine wave and a function of α , from 0 to 360 degrees in azimuth. The amplitude and phase of μ_{CSAre} are a function of the sum of the sines and cosines of the source azimuths. σ_{CSAre} is the square root of a two cycle sine wave and a function of α , from 0 to 360 degrees in azimuth. The amplitude and phase of σ_{CSAre} are a function of the sum of sines and cosines of the angle of the source azimuths and the sum of the sines and cosines of the double angle of the source azimuths.

σ_{CSAre} evaluated with $P_e = 1$ is defined as the source projection geometric factor, SF. This is different from HDOP. HDOP does not depend on the position error angle, α , but only on the source azimuths, $\theta(k)$. SF, in contrast, is a function of α and the source azimuths, except for a special case described below. SF is less than $\sqrt{K/(K-1)}$ and approaches $1/\sqrt{2}$ as the number of sources distributed

around the navigation point increases, while HDOP can increase without bound for geometries in which source azimuths coalesce, as can be seen in Fig. 2 for points outside the source constellation. There is a special case for which there is a simple analytical relationship between HDOP and SF; this case is a source geometry that has an equal distribution in azimuth around the navigation point of $360/K$, for $K > 1$. For this geometry, the mean, $\mu_{CSAre} = 0$ and $SF = \sqrt{K/2(K-1)}$, are both independent of α . HDOP is simply $2/\sqrt{K}$, and therefore, $SF = (1/HDOP)\sqrt{2/(K-1)}$, and there is an inverse relationship. The equi-distribution of sources around an area of interest is, in fact, a good geometry for navigation ($K > 3$), and although this simple relationship only works exactly at one position, HDOP is somewhat weakly dependent on position as long as one stays inside the constellation, as can be seen in Fig. 2. SF, however, is no longer a constant and has the sinusoidal dependence on α , i.e., with a value that changes with the azimuth of the position error. In Fig. 9(a), the spread of the data is the result of the modulation of each point by the changing value of SF with the actual error azimuth of each position (not captured by HDOP), as well as, the number and position of the PhilSea10 sources actually used for the position calculation (captured by HDOP). For arbitrary source geometry constellations where HDOP is approximately equal to or less than 1 inside the constellation, a good approximation of HDOP is given by $2/\sqrt{K(1-s^2)}$ and the average of SF is given by $\sim \sqrt{K(1-s^2)/2(K-1)}$, where “s” is the square root of the sum of the squares of the mean of sines and mean of the cosines of the source azimuths.

Figure 9(b) shows the projections of the unit magnitude error for each of the six PhilSea10 sources as a function of

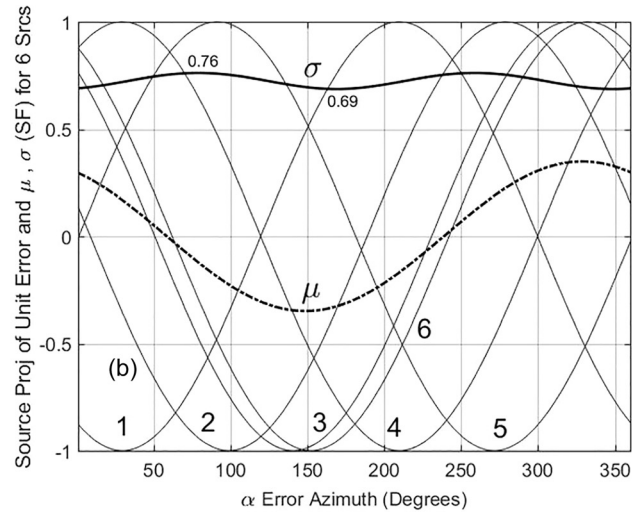
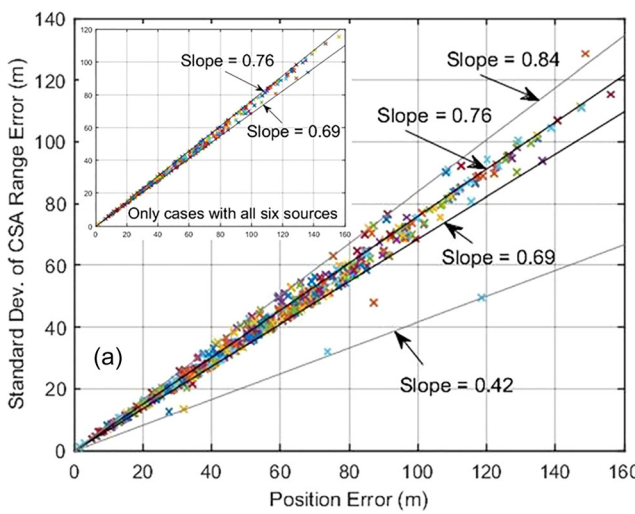


FIG. 9. (Color online) (a) Standard deviation of the K CSA range errors of the K sources used for a given position versus the position error P_e , for that position. All 502 positions are plotted. The slopes of the lines correspond to computed values of the source geometry factor SF. For $K=6$ sources (1–6) 0.76 is the maximum and 0.69 is the minimum. The slope of 0.84 is the maximum for $K=5$ sources (1–5), and 0.42 is the minimum for $K=5$ sources (2–6). The slope of the best fit line for all 502 points is 0.76 (coincidentally). The inset in the upper left is the plot of only those positions that used all six sources that were 380 of the 502 positions. There are no outliers. (b) shows the source projections for unit vector position error as a function of the azimuth angle, α , of the error from 0 to 360 degrees, with the sine waves marked according to source number. The upper solid black line marked σ is SF, the standard deviation of the source projections, given by Eq. (6) with $P_e = 1$. The calculation shown in (b) is for sources 1–6 showing the SF maximum of 0.76 and the minimum of 0.69. The lower black dashed-dotted line marked μ , is the mean of the source projections, given by Eq. (5).

the position error azimuth α , from 0 to 360 degrees. μ_{CSAre} and σ_{CSAre} computed for $K=6$ (all six sources in the PhilSea10 constellation) and $P_e=1$ ($\sigma_{CSAre} \equiv$ SF) are shown as the lower and upper black lines, respectively. SF (the upper black line labeled “ σ ”) in Fig. 9(b) has a maximum of 0.76 and a minimum of 0.69. For each position marked with “x” in Fig. 9(a), P_e for that position is multiplied by SF evaluated at the error azimuth, α , for that position. Thus the “x’s” fall between the maximum and minimum values of SF times P_e and, therefore, within the slopes given by the maximum and minimum of SF when plotted against P_e . The “x’s” above 0.76 and below 0.69 in Fig. 9(a) are cases where all six sources were not available. The 0.84 line is the maximum value of SF calculated for sources 1–5, as was the case for 104 of the positions after source six stopped transmitting on Julian day 305. The 0.42 line is the minimum of SF calculated for sources 2–6 when source 1 was missing during the first transmission on Days 191 and 197. The best fit slope for all the positions in Fig. 9(a) is 0.76, coincidentally close to the maximum amplitude for the $K=6$ calculation shown above. The upper left inset in Fig. 9(a) is a plot of only those positions that had six sources, of which there were 380, and as expected, they all fall between the min and max of SF (>0.69 and <0.76). The calculation of SF was done for the DVLA anchor position and not the actual position. Given that the watch circle was at most several hundred meters from the anchor position, the difference between SF calculated at the actual position and the anchor position is negligible, namely, the difference of the source azimuth, θ , calculated for the anchor position versus for the true position. SF will also be important when calculating the observation errors and the standard deviation of the group speeds, \hat{c}_g^k , as a function of the position error P_e .

The position error, P_e , is plotted versus the standard deviation of the *observation* range errors in Fig. 10. The correlation coefficient is 0.61, but there is no linear relation with P_e as there is with the CSA range errors. There is an upper bound on P_e as a function of the standard deviation of the observation range errors equivalent to the CSA range errors that is given by the best fit line from Fig. 9(a) (close to the mean of SF when all positions are used including those without all six sources). That is, P_e can be less than but not greater than the standard deviation of the observation range errors multiplied by SF. The observation range error can never be less than the CSA range error, as can be seen in Fig. 6. In the limit as the LS fit errors, the residuals, go to zero, the observation ranges are equal to the CSA ranges, and therefore the observation range errors equal the CSA range errors (the observation range error equals the CSA range error plus the residual). However, the minimum LS fit, residual standard deviation was 7 m, and only seven positions were less than 20 m, and the residuals can get quite large (~ 200 m), which explains why the observation range error standard deviation extends above the CSA range error standard deviation and also why the lower bound in Fig. 10(a) is closer to the larger mean value of the CSA range error standard deviation and not the minimum value of the

CSA range error. The black x’s show the binned average of P_e at a constant standard deviation of the observation errors versus the standard deviation of the observation errors with the average done ± 5 m, from 20 to 120 m at 10 m increments. The line with the slope 1/HDOP times $2/\sqrt{\pi}$ is where P_e equals the standard deviation of the observation range error multiplied by HDOP times $(1/2)\sqrt{\pi}$. Because HDOP times the standard deviation of the observation range error is equal to the 2-D rms error, the $(1/2)\sqrt{\pi}$ factor is needed to convert the 2-D rms error to P_e on the x axis. This slope is very close to the best fit. The mean of the 502 standard deviations of each of the K sources for all 502 positions in Fig. 10(a) is 76 m, very close as expected to the standard deviation of all 2888 observation range errors of 77 m shown in Fig. 7(a). This shows that HDOP does provide a good estimate of the position error (2-D rms, or “equivalently” P_e), while SF provides an upper bound on the position error.

In Fig. 10(b), the standard deviation of \hat{c}_g^k for the K sources for each position is plotted versus P_e and has a correlation of 0.53. Because \hat{c}_g^k is equal to the ground truth range divided by the EOC travel time, t^k , recomputing Eqs. (5) and (6) by dividing the unit projection error [the cosine term in both Eq. (5) and (6)] by t^k gives the SF “for group speed,” denoted SFc. It is the square root of the two cycle sine wave, and for the PhilSea10 six-source geometry has a minimum equal to 0.0041. For the 1–5 source geometry after source 6 failure, the minimum is 0.0033. The corresponding slopes are shown in Fig. 10(b). While SF is dimensionless, SFc has units of s^{-1} , and the inverse of the mean of SFc is approximately equal to the average travel time from the sources. For the six-source geometry, the mean of SFc is 0.0049 with inverse equal to 204 s and the average travel time is 201 s. For the five source geometry without source 6, the inverse is 244 s and the average travel time is 224 s.

The standard deviation of the group speeds from the sources used in the CSA algorithm for any given position divided by SFc is an upper bound on the position error P_e . As will be discussed in Sec. III D, the standard deviation of \hat{c}_g^k is comparable to the standard deviation of the group speed computed from each source using the PhilSea10 ocean model. This presages the possibility of predicting CSA performance of a notional source constellation from which SFc is computed with an ocean GCM and an acoustic propagation code to compute the standard deviation of the group speeds and the t^k . Clearly, the accuracy of the ocean GCM will determine if this is possible.

Without ground truth, the only position performance measures available are the residuals of the least squares position fit, or the LS fit range errors. The standard deviations of the residuals, σ_o , for each of the 502 positions, were calculated. Figure 11(a) is a scatter plot of the actual position error with the corresponding σ_o . There is no significant correlation between σ_o and the actual position error, P_e . Statistically, however, they are similar with a mean error of 77 m and a standard deviation of 39 m for σ_o , versus a mean error of 58 m and a standard deviation 32 m for the actual

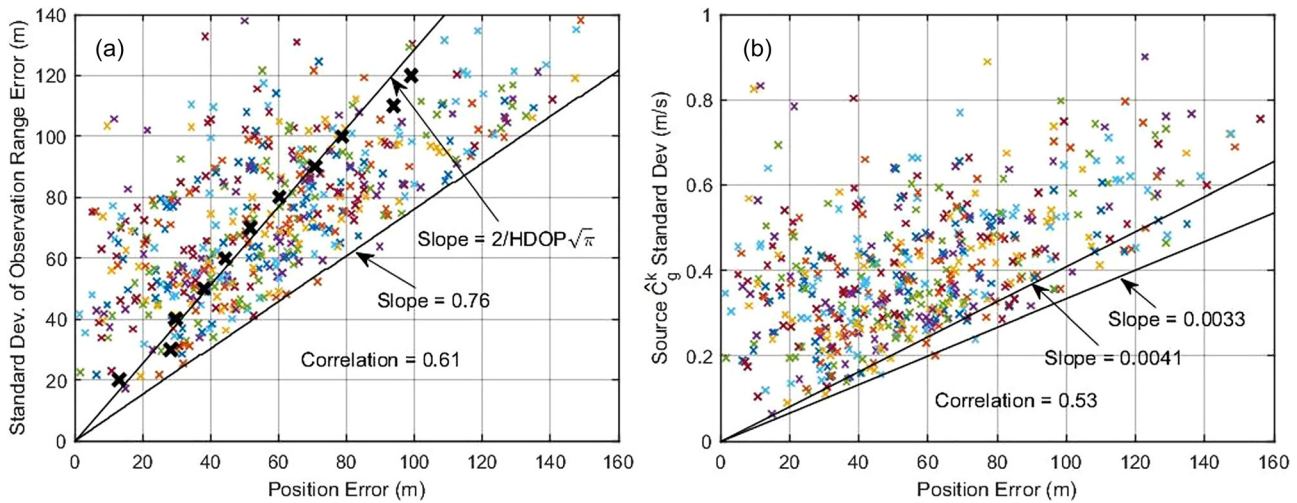


FIG. 10. (Color online) (a) Shows the standard deviation of the K observation range errors of the K sources used for a given position versus position error P_e for that position. All 502 positions are plotted. The line with the slope of 0.76 (the average of SF for all the source configurations used) shows an upper bound of the position error P_e . The number of positions with the three source configurations with K sources was, for $K=6$ (380 positions), $K=5$ (120 positions), and $K=4$ (2 positions). The line with the slope of $1/\text{HDOP}$ times $2/\sqrt{\pi}$ is shown. The black x's are the average of P_e versus the standard deviation of the observation errors as described in the text. (b) shows the standard deviation of the group speeds, \hat{c}_g^k , for the K sources used for a given position versus P_e for that position. The lines with slope of 0.0041, the minimum of SFc for $K=6$ sources, and with slope of 0.0033, the minimum of SFc for $K=5$ sources, are shown.

position errors. Figure 11(b) is a plot of all the LS fit range errors (residuals) and a Gaussian with the measured mean of 6 m and standard deviation 61 m. It is non-Gaussian with a skewness of -0.4 and a kurtosis of 5. The standard deviation is close to the actual mean position error and the actual 2-D rms error. Of interest is that the standard deviation is independent of range as shown in Fig. 8 (the dotted lines), though the mean errors are quite large. Since it is the variability of the c_g^k from source to source for each position that clearly impacts the CSA least squares fit, perhaps it is not surprising that the statistics of the residuals are similar to the actual errors, and the statistics of the residuals are likely

useful for estimating performance when ground truth is not available.

B. CSA positions over the year of PhilSea10 and compensating for the mesoscale

The CSA position errors will depend on the variation of the standard deviation of the group speeds as a function of time. In Fig. 12, the average position error, P_e (black "o's"), and the corresponding standard deviation of the position error (blue "x's") of the eight transmissions received on one day on each hydrophone processed are plotted as a function

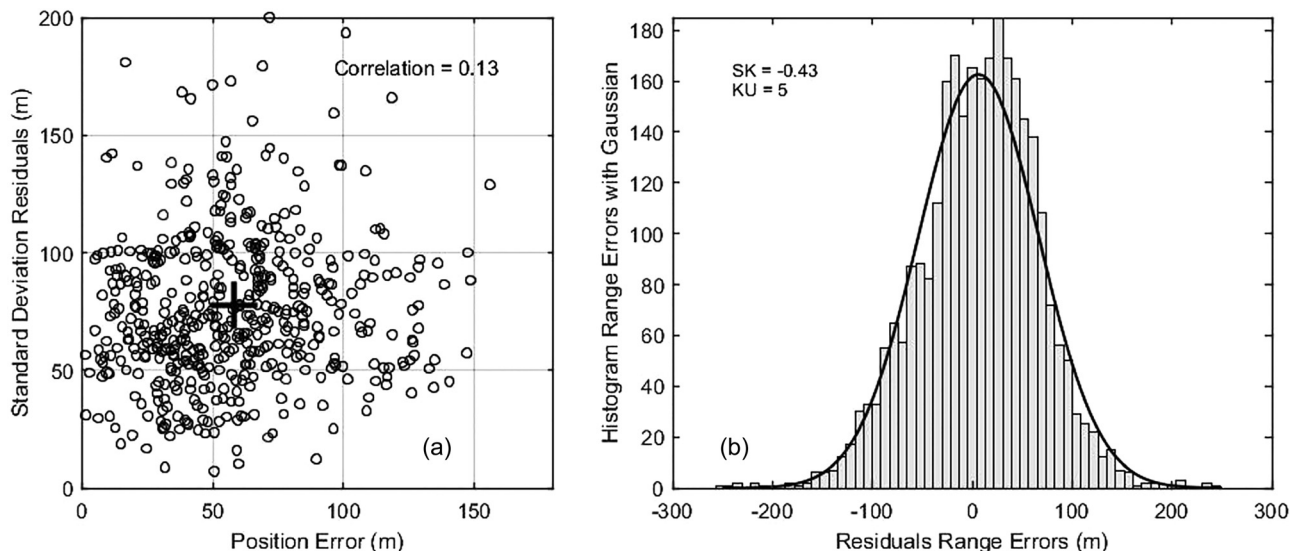


FIG. 11. (a) Shows standard deviations of the least squares fit range errors (residuals), σ_o , for 502 positions color versus P_e . The black "+" is plotted at the mean of $\sigma_o = 77$ m and the mean of $P_e = 58$ m. (b) Shows the 2888 least squares fit range errors (residuals) histogram plotted with a Gaussian with measured mean of 6.2 m and measured standard deviation of 61 m.

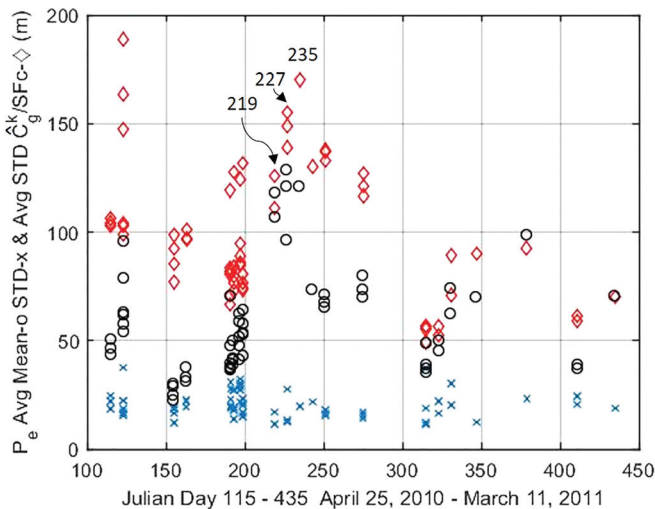


FIG. 12. Position error as a function of Julian day from day 115 through day 435. The P_e (black circles) are computed for the particular hydrophones in the DVLA processed on the day shown. Each black circle is the average of that hydrophone's P_e over the eight transmissions of the day. The blue x's are the standard deviation of P_e , and the red diamonds are the standard deviation of the \hat{c}_g^k/SFC , also averaged over the eight transmissions of the day for each hydrophone processed that day.

of Julian day over the year of the PhilSea10 experiment. To explain what is being averaged, recall Fig. 4, which shows all eight positions and the tidal watch circle track for the day at the hydrophone at 565 meters depth on Julian day 197, 16 July 2010. The mean of P_e is 41 m and the standard deviation is 22 m for these eight positions and that is what is plotted in Fig. 12 on Julian day 197, along with the averages of the other four hydrophones/depths that were processed on that day. There were 63 hydrophone-tracks like Fig. 4 generated for PhilSea10 providing 63 average P_e and standard deviation points for the plot. The red diamonds are the corresponding average of the standard deviation of the \hat{c}_g^k for each of the eight positions divided by the SFC factor of 0.0041, and are approximately equal to or greater than P_e , as also shown in Fig. 10(b). Figure 12 shows the variability of CSA performance over the year of the PhilSea10 experiment. This variation is the result of the changes in the c_g^k caused by strong mesoscale eddies, fronts, and tidal currents that are prevalent within the PhilSea10 source constellation.⁹ A slice of the sound speed at the axial depth of ~ 1027 m for day 227, 15 August 2010, from the tomographically-constrained ocean model shown in Fig. 13 illustrates the horizontal spatial variability and scale of the sound speed between each of the sources (o's) and the DVLA, "x."

As shown in Fig. 12, days 219, 227, and 235, (7, 15, and 23 August 2010), respectively, show the highest mean P_e of the year. The standard deviation of P_e , however, is fairly constant throughout the year. For most cases, even when the mean P_e was high, the shape of the drift watch circle was accurately tracked (low standard deviation), but was shifted as shown in Fig. 14(a). The track of the eight positions for day 227 for the hydrophone at 1035 m depth (the highest position error in the data set) is shifted to the

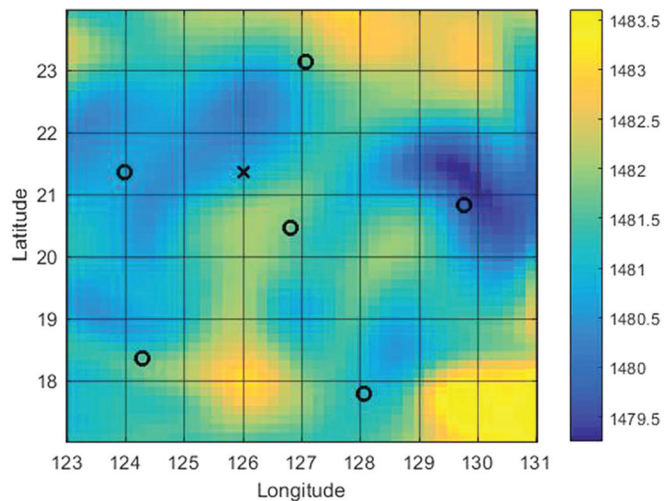


FIG. 13. A slice of the PhilSea10 tomographically-constrained ocean at a depth of 1027 m near the axis of the sound channel on 15 August 2010 showing the horizontal variations of sound speed between the sources (o) and DVLA(x).

southwest. The standard deviation of the \hat{c}_g^k (red diamonds in Fig. 12) are among the highest in the record.

If the actual c_g^k were known, the time shift for each source to correct for the difference between c_g^k and c_g^{CSA} , could be calculated

$$\Delta t^k = (c_g^k/c_g^{CSA} - 1)t^k. \quad (7)$$

In Fig. 15, \hat{c}_g^k is plotted for each transmission and each source (numbered lines) on day 227, as is c_g^{CSA} (the dashed line) and the mean of the \hat{c}_g^k (the dotted-dashed line). The averages of the group speeds for each source over all eight transmissions are shown in the lower right of the figure, as well as the calculated Δt^k in seconds using \hat{c}_g^k in Eq. (7). In Eq. (3), t^k is replaced with $t^k + \Delta t^k$, and the least squares solution is computed again. Because \hat{c}_g^k was defined as the ground truth range divided by t^k , the solution with all the Δt^k corrections as shown in Fig. 14(b) gives a solution close to the ground truth, as would be expected. In fact, it would be exact if the corrections were applied for each transmission separately rather than using the average for all eight transmissions. The important point is that the major error associated with the CSA is the assumption of the single sound speed, and if the actual group speeds can be determined for the travel time selected in the arrival pattern then a much more accurate position can be calculated. Estimating the Δt^k from the data by using the bulk shift correction (which will be discussed below in Sec. III E) and multiplying by c_g^{CSA} is in fact estimating the CSA range error for the k^{th} source and is one way to mitigate this error. These are corrections for the mesoscale and tidal variability (assuming errors associated with internal waves are small in comparison). An ocean GCM including tides with tomographic constraints should be able to provide sufficiently accurate modeling results to compute these corrections.

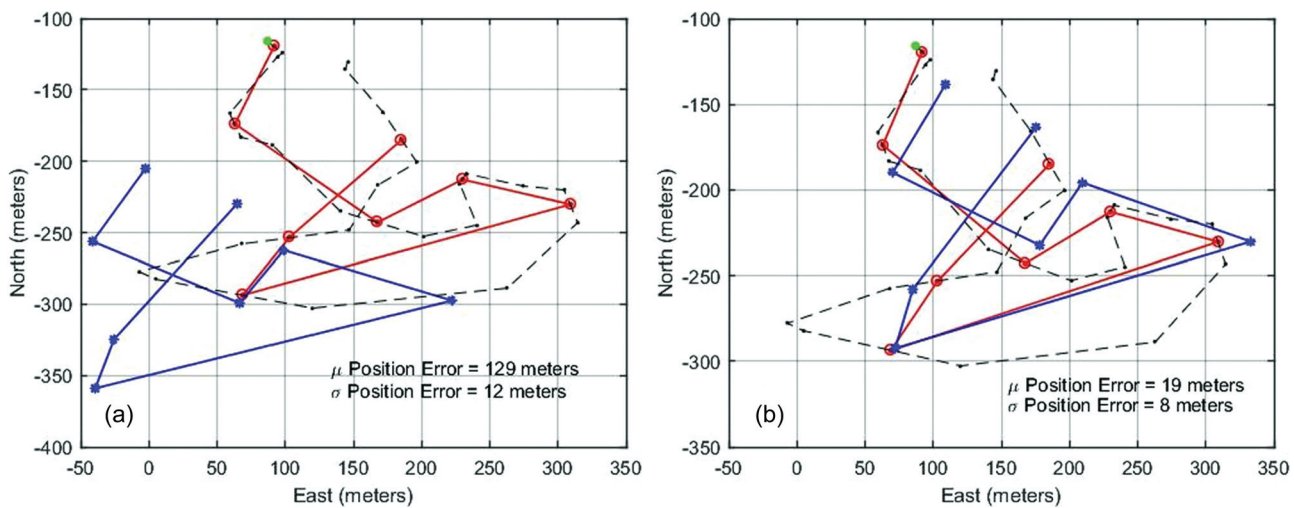


FIG. 14. (a) Shows the CSA positions (blue) and ground truth (red) for the hydrophone at depth of 1035 m on day 227, 15 August 2010. (b) Shows the CSA positions using the corrected travel time $t^k + \Delta t^k$ for each of the sources (blue), as described in the text, with the ground truth (red).

C. CSA/PhilSea10 and navigation applications

From the standpoint of source and receiver ground truth (~ 1 m), travel time measurement precision ($\sim 1\text{--}3$ ms), SNR, and HDOP at depths between ~ 500 and 3000 m, the PhilSea10 data set is an excellent one for testing the CSA performance. There are some additional limitations that affect overall position accuracy that can clearly be improved for a system specifically designed for navigation. Hydrophone motion during the 45 min time required for transmissions from all six sources to be received, as shown in Fig. 4, results in multiple tens of meters of error. Source transmissions on higher repetition rates than minutes to reduce the latency of receiving all source transmissions for a position calculation and increasing the transmission sequence rate to minutes

vice hours to reduce the time between fixes is needed. Implementation of the CSA in a Kalman filter smoother/tracker that incorporates vehicle dynamics/motion and on-board inertial navigation system data is also required for operational vehicles. Furthermore, a higher rep rate would improve the ability to track rays through fades, as well as use automated tracking of rays as developed by Dzieciuch.¹⁷ Doppler must be accounted for with waveforms that are not Doppler tolerant. For the LFM waveforms that were used in PhilSea10, Doppler compensation is required depending upon the velocity of the vehicle. The relative motion of the DVLA and source arrays was $<3\text{--}4$ cm/s with a corresponding time correction of <8 ms or <10 m position error, and Doppler compensation was not deemed necessary at the current level of 58 m mean position error.

The largest factor in the position error of the CSA is the error associated with the assumption of a single sound speed, as discussed above. The analyses of these data show that, while the position error P_e is bounded by the standard deviation of the source group speeds c_g^k , as estimated by \hat{c}_g^k , shown in Fig. 10(b), the position error cannot be guaranteed to be better than the standard deviation divided by SFc, and this was as large as 150 m for the Philippine Sea data. The good news is that this error bound can be calculated and corrections can be made to reduce the standard deviation of the group speeds c_g^k [or directly account for these group speeds as illustrated in Fig. 14(b)], lowering the upper bound of the position error. Likewise, the accuracy of the CSA in other oceans can be computed if measurements or estimates of c_g^k can be made.

Internal waves also affect the CSA performance and will ultimately be the limit of navigation performance after successfully correcting for the mesoscale and tidal variation. Internal waves will be statistically independent from source to source, assuming a source separation that would also provide good HDOP, and the averaging inherent in the least squares calculation will help, but it is not obvious what the magnitude of this error is. Correcting for the variations in c_g^k

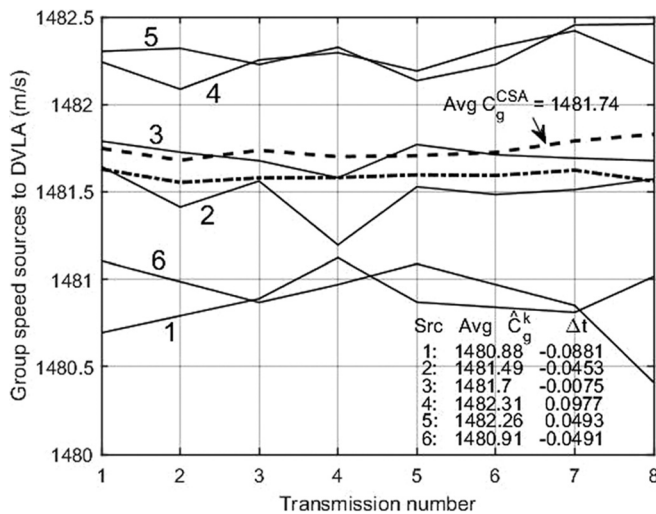


FIG. 15. The group speeds, \hat{c}_g^k , for sources 1–6 plotted versus the transmission number on day 227 and hydrophone depth of 1035 m. The c_g^{CSA} for each transmission is the dashed line with the average for day 227 of 1481.74 m/s. The mean of the \hat{c}_g^k for each transmission is the dotted-dashed line. The average \hat{c}_g^k for each source for the eight transmissions on day 227 is shown in the lower right table followed by the Δt^k in seconds for each source using the average c_g^{CSA} and average \hat{c}_g^k in Eq. (7).

can remove the large P_e shifts evident in Fig. 12. The fairly stable standard deviation (mean = 21 m and standard deviation = 6 m) shown in Fig. 12 certainly has elements of the transmission sequencing navigation errors but could be indicative of an internal wave performance floor. Likely, this will not be fully revealed until a well-designed navigation experiment is conducted that will peel back the meso-scale and tidal onion to see what is left.

D. CSA group speed

The c_g^{CSA} is approximately equal to the group speed of the mode/ray whose turning depth is the hydrophone depth, as a result of selecting the EOC time as the source travel time, t^k , in Eq. (3). The c_g^{CSA} computed for nine hydrophones in the DVLA for day 197 is plotted as a function of the receiving hydrophone depth in Fig. 16. The “X’s” are the average of the c_g^{CSA} over the day as described below to remove tidal modulation. The blue line is the computed group speed from the KRAKEN acoustic normal mode propagation code using a range-dependent adiabatic approximation plotted as a function of the mode turning depth using the ocean model for this day. The calculation

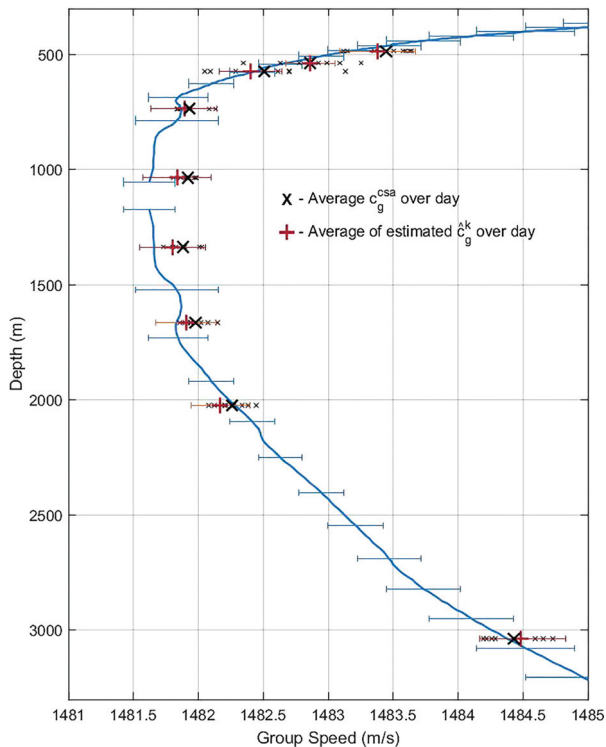


FIG. 16. Group speeds plotted as a function of turning depth (blue) on day 197 using the KRAKEN mode code with adiabatic modes and the range-dependent tomographically-constrained PhilSea10 ocean model. The blue error bars are ± 1 sigma of the variation of the group speeds from each of the six sources. The small black ‘x’s are the c_g^{CSA} , calculated for the eight transmissions of the day for each of the nine hydrophones plotted at the depths of the hydrophones (485, 537, 574, 735, 1035, 1335, 1664, 2024, and 3037 m). The large X’s are the average over the day of the eight c_g^{CSA} , for comparison to the calculated mode group speeds. The red +’s are the means of the group speeds, \hat{c}_g^k . The red error bars are the ± 1 sigma of the variation of the group speeds, \hat{c}_g^k , calculated for each source and also averaged over the eight positions/transmissions of the day.

computes the range-average group speed for each source-receiver path, and the blue line is the average of the six source-receiver paths. The blue error bars are $\pm 1\sigma$ of the source-to-source variability and are ~ 0.2 – 0.3 m/s with some depth dependence. The ocean model is the 4-D ocean for the PhilSea10 experiment constrained by the tomography.¹³ Because this model does not include tides, the c_g^{CSA} denoted by the “X” is the average of the c_g^{CSA} computed for each of the eight source transmission sequences during a single day which are shown by the small “x’s” in Fig. 16. The c_g^{CSA} computed from the data and the calculation of the group speed from the ocean model are independent calculations. The agreement is good. Using the EOC travel time “filters” the travel time measured from each source to be the travel time of the ray/mode with the same turning depth for each source at the depth of the receiving hydrophone and thus approximately the group speed at the depth of the hydrophone (i.e., vehicle depth). This source-to-source uniformity in selecting the travel time helps reduce the standard deviation of the source group speeds relative to the single sound speed that is assumed and improves the CSA performance over using earlier arrivals in the arrival pattern. Using the maximum peak in the arrival pattern, the first arrival, or an average arrival time resulted in worse performance by as much as hundreds of meters.

However, using the CSA position, acoustic modeling can be performed and ray/mode identification can identify specific earlier arrivals and their group velocity to directly account for the different group speeds in the observation equations [Eq. (3)], as is done in GNSS. Using information from the full arrival pattern will improve the position estimate. CSA position accuracy is limited by the difference between the single c_g^{CSA} and the “actual” group speed from each source, c_g^k , at the receiver depth, that in fact is not well defined without an accurate ocean model and propagation code discussed above. As shown above, the CSA position error is directly proportional to the standard deviation of the estimated group speeds of the K sources used for that position.

While the agreement between model and data shown in Fig. 16 is good, the c_g^{CSA} is faster near the sound channel axis than the group speeds computed using the KRAKEN adiabatic modes with the range-dependent ocean model by ~ 0.25 m/s. The Bowlin RAY code can also be used to model the group speeds by taking the known actual range from ground truth and dividing by the time of arrival of the wave fronts generated using the same 4-D ocean that provided the range-dependent sound speed used for the adiabatic mode calculation as shown in Fig. 17. The ray calculated group speed is also faster than the adiabatic mode calculation. However, there were adiabatic model and ray model differences for individual source paths, with two of the paths (sources 2 and 3) showing almost no difference near the axis, as shown for source 2 in Fig. 17. The paths from the other sources show faster group speeds near the axis varying by ~ 0.15 to 0.35 m/s from the ray model. This could be a result of the fact that tidal effects are not in the

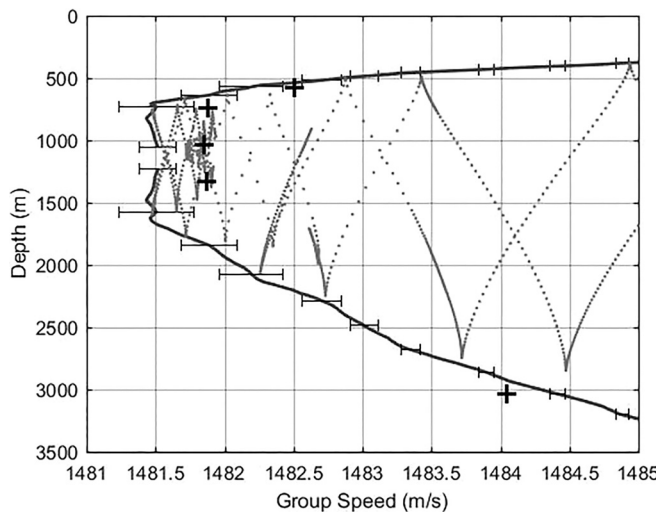


FIG. 17. Bowlin RAY code group speed of wave fronts (grey dots) for source 2 with the group speed of the adiabatic modes versus mode turning depth (black solid line) calculated from KRAKEN for day 197. The error bars are ± 1 sigma of the variation of the group speed along the path from source 2 to the DVLA. The black '+'s are the average \hat{c}_g^k over the eight transmissions of the day for the hydrophones at 537, 735, 1035, and 3037 m.

model, but these specific modeling discrepancies are not fully understood.

The c_g^{CSA} for each position is plotted in Fig. 18 versus the average of the K sources' \hat{c}_g^k group speeds used to compute that position for all positions computed. The correlation is 0.99. The higher group speeds in the cluster at the upper right hand side of Fig. 18 are all from the one deepest depth hydrophone processed at 3037 m and the c_g^{CSA} are generally less than the mean of the \hat{c}_g^k (above the solid line). However, as can be seen from the plot, for the group speeds near the axis (< 1482 m/s on the x axis of Fig. 18), the c_g^{CSA} are generally approximately equal to or greater than the mean of the estimated actual group speeds for each position (below the

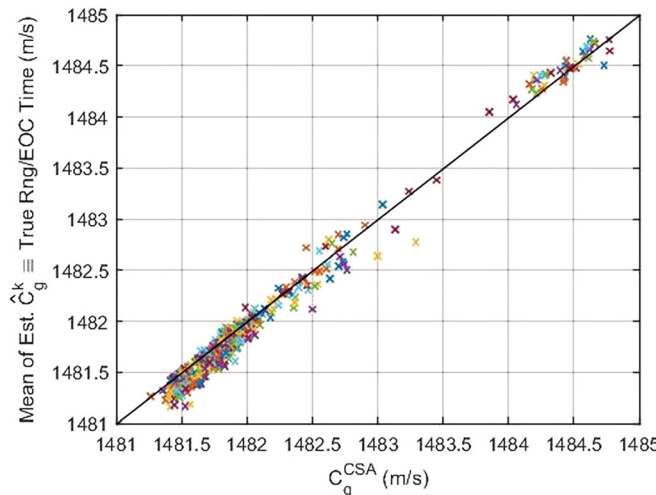


FIG. 18. (Color online) For each of the 502 positions, the mean of the group speeds of the K sources, \hat{c}_g^k , used for the position is plotted against the c_g^{CSA} , for that position. The solid line is the mean of $\hat{c}_g^k = c_g^{CSA}$.

solid line). For day 197, the average of all sources' \hat{c}_g^k for all eight transmissions is plotted in Fig. 16 (the red '+'s) along with the corresponding red error bars for $\pm 1\sigma$. The 1σ standard deviation of the measured \hat{c}_g^k , the red error bars, are comparable to the 1σ of the adiabatic group speed computed from the ocean model, the blue error bars. This implies that an estimate of the standard deviation of the group speeds could potentially be calculated directly from the ocean model. The measured \hat{c}_g^k , while slower than the c_g^{CSA} , are still faster than the computed group speeds from the ocean model. The measured \hat{c}_g^k for each source path are calculated and shown for source 2 in Fig. 17, where the black '+'s are the mean over the eight transmissions during the day. The axial and shallower depths show faster group speeds than the adiabatic model, while the deepest depth shows a slower group speed. Sources 3 and 4 show similar results as 2, except the deepest depth shows good agreement. Sources 5 and 6 show good agreement at all depths, while source 1 shows slower sound speeds than the adiabatic model results. It should also be noted, as shown in Fig. 17, that the axial arrivals can be quite complex. It is apparent in Fig. 17 that the last arrivals are from a mode/ray that turns above the axis at ~ 750 m. The axial energy appears to arrive approximately 30 ms earlier at the correspondingly higher group speed. Often these last peaks in the pulse compression time series are small and not well defined but are detectable in many cases. Whether or not the EOC auto-detect picks the actual ray/mode that turns at the hydrophone receiver depth only affects position performance if the error is large enough to significantly increase the standard deviation of the \hat{c}_g^k . The performance results to date indicate that these EOC detection errors are small compared to the oceanic variability.

Resolving the differences in group speeds calculated from the models, when compared to the CSA processed data, c_g^{CSA} , and \hat{c}_g^k (using the measured EOC time and the ground truth range), is needed to fully understand what and how model aided improvements can be realized for the CSA-based navigation performance. These differences must result from either (i) differences in the ocean model from the actual ocean, (ii) propagation modeling deficiencies, or (iii) possible biases in the EOC travel-time detection. Measuring the EOC travel time is not straightforward. Missing final arrivals as discussed above lead to a faster travel time and a correspondingly higher group velocity that directly affects c_g^{CSA} and \hat{c}_g^k , which could explain some of the differences shown in Fig. 16. Additionally, because the acoustic propagation model calculation used the adiabatic assumption, mode coupling in the data, where higher faster modes are coupled into and out of lower axial modes, is not accounted for, leading to possibly higher measured c_g^{CSA} and \hat{c}_g^k . This axial and near-axial speed up has been seen in simulations recently reported by Baggeroer;¹⁸ however, this calculation used a range-independent Munk profile with internal-wave modulation of the sound speed causing the coupling. The range dependent Bowlin RAY code should, however, accurately capture the ray travel times for distinct

paths, although that is admittedly problematic near the axis. Further investigation including propagation modeling with internal wave modulation of a range dependent set of profiles, for example, from the PhilSea10 ocean model, is needed.

E. Future work

The use of the CSA position for acoustic modeling with the sound-speed field from tomography to improve the position estimates could meet or exceed the ~ 50 m accuracy potential hypothesized by Duda *et al.*⁴ and the ~ 58 m mean CSA results demonstrated with the PhilSea10 data. This can be done in two ways. First, the c_g^k can be estimated using an ocean GCM and propagation code and applied directly in Eq. (3) or as a correction to each source arrival time using Eq. (7). The modeling inconsistencies noted above in Sec. III D need to be understood before this method is likely to be consistently successful. The second method is to estimate the Δt^k directly using the data and the modeled arrival pattern from the source to the CSA position. This has been tested for eight positions for day 197 with a hydrophone on the DVLA at 565 m depth using the bulk shifting technique described by Van Uffelen *et al.*,⁶ and with further recent analysis in Wu *et al.*¹⁹ The initial CSA position error had a mean of 41 m and a standard deviation of 22 m for the eight positions that day. The arrival pattern at the CSA position was computed using the PhilSea10 tomographically-constrained ocean model and the Bowlin RAY propagation code. These modeled arrival patterns were compared to the measured arrival patterns for each source to determine the Δt^k time offset, or bulk shift of the arrival pattern, which can be negative or positive. The range offsets given by $\Delta t^k \times c_g^{CSA}$ is an estimate of the CSA range errors from the actual position for each of the sources. The corrected travel time is $t^k + \Delta t^k$ for each of the sources. The least squares algorithm was run again with the corrected EOC times and was implemented by solving for the new (x, y) position using the previously computed c_g^{CSA} , i.e., two unknowns, and also by solving for c_g^{CSA} again, with three unknowns. For this case, both methods were close. The mean position error was reduced to 27 m, and the standard deviation reduced to 16 m for the eight positions. This method was also applied to Day 227 for the hydrophone at 1035 m depth shown in Fig. 14(a). The mean error was reduced from 129 to 36 m and the standard deviation slightly increased from 12 to 14 m. On-going work and the subject of a follow on paper will determine if this result is supported with a complete analysis of the data set. Implementing the CSA and model-based CSA improvements within a Kalman filter smoother/tracker is certainly necessary, as are improvements in the automated travel time measurement of the EOC and/or other arrivals.

The CSA overdetermined solution formulation (using no *a priori* estimates) to the underwater navigation problem used in this paper, making a single “c” one of the variables along with the (x, y) position coordinates, was motivated by

GNSS methodology and by the initial results that demonstrated performance much better than anticipated, given the well-known variability of sound speed in the ocean. A possible alternative that will be investigated is a tomographic inversion approach that would include all K group speeds and (x, y) as unknowns making the navigation problem underdetermined, as is common in tomographic inversion problems. The data are the travel times (rather than the product of the travel times and the single computed sound speed), and one does a stochastic weighted least square solution for the sound speeds and position given the travel-time data, allowing for the *a priori* uncertainties in the travel times (data error) and the *a priori* variances in sound speed and position. This was the approach used by Van Uffelen *et al.*,⁶ albeit for a much different formulation of the navigation problem as described in the Introduction that relied on GNSS and vehicle dynamics to determine positions used for acoustic propagation model runs (not required for the CSA) and then estimate offsets from those positions. Similarly, this simultaneous estimation of sound speed with source position errors was also explored in early ocean acoustic tomography work for applications involving the use of moving sources.^{20,21} Both of these papers do joint estimates of sound-speed and the positions of the sources and receivers to determine sensitivity to position errors that in principle could be applied to the navigation problem.

Fundamental improvements in undersea navigation will require better understanding of the ocean sound-speed structure and its evolution in space and time. GCMs are getting more and more accurate with the higher resolution needed to support acoustic modeling calculations. The trend is in the right direction. Improvements in acoustic source technology, deployment, and operation are also needed to enable CSA and other acoustic-based underwater navigation solutions.

IV. SUMMARY

This paper describes a new simple and robust long-range underwater navigation algorithm with a cold start capability that requires no *a priori* knowledge of position or sound speed to generate a position for underwater vehicles, UUVs, gliders, and floats, without having to surface. The highly dynamic currents, mesoscale, tidal, and internal wave variability of the Philippine Sea⁹ proved to be a good test of the single “c” assumption of the CSA. The data from the PhilSea10 experiment demonstrated mean CSA position errors of 58 m or 0.01%–0.04% of range from the sources with a standard deviation of 32 m. This level of position error is sufficient to navigate floats, gliders, and UUVs for sampling the ocean dynamics of the mesoscale fronts and eddies, tides, and shorter period processes at smaller scales of a few kilometers.⁴ This position is also accurate enough that it can be used for acoustic modeling with an ocean GCM to possibly improve the position accuracy for other applications. An upper bound on CSA navigation error using SFc is defined. If sufficiently accurate estimates of the c_g^k

can be extracted from GCMs or ocean measurements, both the rms position error and upper bound of the position error can be predicted. The algorithm is inherently scalable from a LBL geometry to larger ranges subject to the requirement for a suitable low HDOP acoustic source constellation (i.e., enough well positioned sources and sufficient SNR illumination for high precision travel time estimation). Navigation performance for source ranges in excess of 450 km is required to determine if large areas of the ocean can be covered efficiently with acoustic sources for underwater navigation. The focus of this work is on long range and long term submerged GNSS denied undersea positioning.

ACKNOWLEDGMENTS

P.M. developed the UNA/CSA and the automated EOC detection code, processed and analyzed the PhilSea10 data to obtain the performance results and their relationship with GNSS performance measures, derived the SF and SFc source geometry factors and their relationship to HDOP, and wrote the original manuscript. M.D. and P.W. provided the PhilSea10 data and meta-data that made testing of the UNA/CSA possible and provided significant editorial support. B.S. assisted with data acquisition codes and acoustic modeling, including providing the Bowlin RAY code. K.W. computed the group speeds using the KRAKEN propagation code with the 4-D ocean GCM and the PhilSea10 source/receiver geometry for comparison with the CSA computed group speeds. P.M. thanks Leidos, Inc. and the Maritime Systems Division of Leidos, Inc. for the support of this work including the algorithm development and an exploratory IRAD to test the algorithm with the Philippine Sea Data. Thanks to Robert Headrick at the Office of Naval Research (ONR) for permission to use the data from the ONR funded Philippine Sea 2010–2011 North Pacific Acoustic Laboratory experiment. Thanks to Ganesh Gopalakrishnan and Bruce Cornuelle who provided the 4-D ocean GCM constrained by tomography for the Philippine Sea covering the PhilSea10 experiment area. Thanks to Arthur Baggeroer, Professor Emeritus, MIT, who provided the initial DVLA data and many valuable comments along the way and reviewed the manuscript. P.M. thanks Leidos colleagues Zachary Guralnik, Kritika Vayur, and Chuck Spofford for their support, impromptu discussions, insightful observations, and encouragement throughout this effort. The authors thank the anonymous reviewers for their comments and recommendations.

¹T. Rossby, D. Dorson, and J. Fontaine, “The RAFOS system,” *J. Atmos. Ocean. Technol.* **3**(4), 672–679 (1986).

²See for example, VectorNav Technologies Report, “Inertial Navigation, Unaided Position Estimate,” <https://www.vectornav.com/support/library/imu-and-ins>.

³L. Paull, S. Saeedi, M. Seto, and H. Li, “AUV navigation and localization: A review,” *IEEE J. Oceanic Eng.* **39**(1), 131–149 (2014).

⁴T. F. Duda, A. K. Morozov, B. H. Howe, M. G. Brown, K. Speer, P. Lazarevich, P. F. Worcester, and B. D. Cornuelle, “Evaluation of a long-range joint acoustic navigation/thermometry system,” in *Proceedings of Oceans 2006*, Boston, MA (September 18–22, 2006), pp. 1–6.

⁵NRC, “Critical infrastructure for ocean research and societal needs in 2030,” Committee on an Ocean Infrastructure Strategy for U.S. Ocean Research in 2030, Ocean Studies Board, Division on Earth and Life Studies (National Research Council National Academies Press, Washington, DC, 2011).

⁶L. J. Van Uffelen, B. M. Howe, E. Nosal, G. S. Carter, P. F. Worcester, and M. A. Dzieciuch, “Localization and subsurface position error estimation of gliders, using broadband acoustic signals at long range,” *IEEE J. Oceanic Eng.* **41**(3) 501–508 (2016).

⁷S. E. Webster, L. E. Freitag, C. M. Lee, and J. I. Gobat, “Towards real-time under-ice acoustic navigation at mesoscale ranges,” in *Proceedings IEEE International Conference on Robotics and Automation*, Seattle, WA (May 26–30, 2015), pp. 537–544.

⁸E. K. Skarsoulis and G. S. Piperakis, “Use of acoustic navigation signals for simultaneous localization and sound-speed estimation,” *J. Acoust. Soc. Am.* **125**(3), 1384–1393 (2009).

⁹P. F. Worcester, M. A. Dzieciuch, J. A. Mercer, R. K. Andrew, B. D. Dushaw, A. B. Baggeroer, K. D. Heaney, G. L. D’Spain, J. A. Colosi, R. A. Stephen, J. N. Kemp, B. M. Howe, L. J. Van Uffelen, and K. E. Wage, “The North Pacific Acoustic Laboratory deep-water acoustic propagation experiments in the Philippine Sea,” *J. Acoust. Soc. Am.* **134**, 3359–3375 (2013).

¹⁰P. N. Mikhalevsky, “Deep ocean long range underwater navigation algorithm (UNA) process for determining the geographic position of underwater vehicles,” U.S. patent application SN15-804695 (November 6, 2017).

¹¹P. Misra and P. Enge, *Global Positioning System: Signals, Measurements, and Performance, Revised Second Edition* (Ganga-Jamuna Press, Lincoln, MA, 2012).

¹²J. B. Bowlin, J. L. Spiesberger, T. F. Duda, and L. F. Freitag, “Ocean acoustical ray-tracing software RAY,” Woods Hole Oceanographic Institution Technical Report No. WHOI-93-10 (Woods Hole Oceanographic Institution, Woods Hole, MA, 1992).

¹³G. Gopalakrishnan and B. D. Cornuelle (private communication, 2019).

¹⁴K. Borre and G. Strang, *Algorithms for Global Positioning* (Wellesley-Cambridge Press, Wellesley, MA, 2012).

¹⁵F. Van Diggelen, “GPS accuracy: Lies, damn lies, and statistics,” *GPS World* **9**(1) 41–45 (1998).

¹⁶F. Van Diggelen, “GNSS accuracy: Lies, damn lies, and statistics,” *GPS World* **18**(1), 2632 (2007).

¹⁷M. A. Dzieciuch, “Signal processing and tracking of arrivals in ocean acoustic tomography,” *J. Acoust. Soc. Am.* **136**(5), 2512–2522 (2014).

¹⁸A. B. Baggeroer, “The arrival time of mode one in a stochastic ocean,” *J. Acoust. Soc. Am.* **144**(3), 1924 (2018).

¹⁹M. Wu, M. P. Barmin, R. K. Andrew, P. B. Weichman, A. W. White, E. M. Lavelle, M. A. Dzieciuch, J. A. Mercer, P. F. Worcester, and M. H. Ritzwoller, “Deep water acoustic range estimation based on an ocean general circulation model: Application to PhilSea10 data,” *J. Acoust. Soc. Am.* **146**, 4754–4773 (2019).

²⁰F. Gaillard, “Ocean acoustic tomography with moving sources or receivers,” *J. Geophys. Res. Oceans* **90**, 11891–11898, <https://doi.org/10.1029/JC090iC06p11891> (1985).

²¹B. D. Cornuelle, W. Munk, and P. F. Worcester, “Ocean acoustic tomography from ships,” *J. Geophys. Res. Oceans* **94**, 6232–6250, <https://doi.org/10.1029/JC094iC05p06232> (1989).